METALLIC HYDROPHOBIC SURFACE FABRICATION AND WETTABILITY STUDY

BY

CONG CUI

A thesis submitted to the school of Graduate Studies in
partial fulfillment of the requirements for the
degree of Master of Engineering

Faculty of Engineering and Applied Science
Memorial University of Newfoundland
May 2018

St John's Newfoundland Canada

ABSTRACT

Hydrophobic surfaces can be designed to have useful properties such as self-cleaning, anti-icing, and flow drag reduction. Research interests in this area have been growing with rising demands from various industries. Hydrophobic surfaces can be fabricated by coating, micro or nano-scale texturing, or a combination of the two. For industrial applications, methods for mass production of hydrophobic surfaces are desired. This thesis investigated two hydrophobic surface fabrication methods, laser machining and sandblasting, and conducted wettability analysis of the fabricated surfaces.

In the laser machining, four microscale surface structures including channel, pillar, varied channel and varied pillar, are designed and fabricated. The static contact angles of all laser-machined samples are close to 130° without any coating. In sandblasting fabrication, three standoff distances (10 mm, 20 mm and 30 mm) between the spray nozzle and target surfaces are tested. For stainless steel, lower standoff distance leads to increased water contact angle on the sandblasted surfaces. For carbon steel, sandblasting increases wettability of the carbon steel, with lower contact angle from lower standoff distance. A low energy coating (Aculon) is applied on the samples from both fabrication methods. In the analysis, samples are divided into two groups, one for coated samples, and the other for the uncoated ones. Overall, the coating increases static contact angle and decreases hysteresis in all laser-machined samples and sandblasted ones.

The difference in wettability of the samples from the two fabrication methods is analyzed in details. Sandblasted samples can reach 113°±4° without any coating, compared with static contact angle of 128°±5° from the laser-machined sample with pillar. After coating, the water

contact angle of sandblasted samples increases to 137°±3° compared with 142°±4° on laser machined samples with pillar. The results of contact angle hysteresis are nearly same for the two methods before coating. After coating, contact angle hysteresis on sandblasted samples is overall lower than that on laser-machined samples.

ACKNOWLEDGEMENTS

I would like to thank my supervisors Dr. Xili Duan and Dr. Kristin M. Poduska for their constant guidance and helps during all stages of this thesis.

I would also like to thank my parents, my wife Yulu Hu for their love and supports. Without them, this work would never have come to existence.

Special thanks and appreciation are given to Petroleum Research Newfoundland & Labrador (PRNL) and to Memorial University of Newfoundland for the financial support, which made this research possible. Thanks are also given to the Faculty of Engineering of Memorial University for providing the resources to carry out this research.

LIST OF ABBREVIATIONS AND SYMBOLS

SEM Scanning Electron Microscope

CA Contact Angle

WEDM Wire Electrical Discharge Machining

MEDM Micro Electrical Discharge Machining

PVB Polyvinyl Butyral

PS Polystyrene

THF Tetrahydrofuran

DMF N-dimethylformamide

LbL Lay-by-Layer assembly method

PDMS Polydimethylsiloxane

PVA Polyvinyl Alcohol

TMOS Tetramethoxysilane

HMDSO Hexamethyldisiloxane

HMDZ Hexamethyldisilazane

AKD Alkylketene Dimer

DR Drag Reduction

PMMA Poly (methyl methacrylate)

PEEK	PolyEtherEtherKetone	
PTFE	Polytetrafluoroethylene	
γ_{SL}	Surface Tension of Solid-liquid Interface	(N/m)
θ_0	Contact Angles of Smooth Surface	(°)
γ_{SV}	Surface Tension of Solid-vapor Interface	(N/m)
f	Contact Area Fraction	
γ_{LV}	Surface Tension of Liquid-Vapor Interface	(N/m)
θ	Contact Angles of Rough Surface	(°)
θ_Y	Young's Angle	(°)
θ_w	Wenzel's angle	(°)
θ_{CB}	Cassie-Baxter's angle	(°)
δ_{CA_Total}	Total Uncertainty	(°)
δ_{CA_Re}	Image Resolution	(°)
δ_{CA_Sd}	Standard Deviation	(°)
r	Roughness Ratio of Real Surface Area to Projected Surface Area	
f_1	Contact area fraction of solid-liquid	
f_2	Contact area fraction of liquid-vapor	
θ_1	Contact angle of solid-liquid	(°)
θ_2	Contact angle of liquid-vapor	(°)

CONTENTS

LIST OF FIGURES

LIST OF TABLES

Chapter 1

Introduction

1.1 Objectives of the Research

Hydrophobic surface has attracted researchers' attention for many years because of its engineering applications such as ice-covering-proof, self-cleaning and drag reduction in fluid flow. Originally from nature inspiration like lotus, various surface structures in microscale and nanoscale are springing up. With deeper investigation in structure dimension effect, scale less than 10μm has been widely studied by many researchers. However, in large microscale region (>100μm), structure impact on wettability also attracts attention in recent years. This thesis compares microscale structures in large scale from laser and in small scale from sandblasting.

The main goals of this research are listed as following.

- To summarize the hydrophobic surface applications and fabrication development.
- To study different methods for static and dynamic contact angle measurement, and investigate factors that affect contact angle measurements
- To discuss the laser method in hydrophobic surface fabrication in pseudo-regular microstructures in large scale.
- To implement sandblasting fabrication to produce hydrophobic surface with random structure in small scale.
- To apply suitable coating on laser machined and sandblasted surfaces and measure their wettability changes.
- To compare samples' wettability performance from different methods

1.2 Methodology

In this research, laser machining and sandblasting method were applied to fabricate hydrophobic surfaces on metal. For laser machining work, four microstructures including channel, pillar, varied channel and varied pillar were laser machined to investigate effects of the microstructures on wettability. In sandblasting work, effects of the standoff distance (10 mm, 20 mm, 30 mm, between nozzle and sample surface) were also analyzed. A low energy coating (Aculon) was applied on samples from both fabrication methods. Static contact angle and hysteresis were adopted to represent wettability. The static contact angle and hysteresis were measured by an OCA 15 contact angle measuring system. Calculated values from Young equation and Cassie model are used to compare with measured static contact angles. The wettability of surfaces from laser machining and sandblasting was compared. SEM (scanning electron microscope) was used to compare the topography of different surfaces.

1.3 Organization of Thesis

Chapter 2 provides an overview of hydrophobic surface and basic knowledge of wetting. Three applications of hydrophobic surfaces are reviewed. Some hydrophobic surface fabrication methods are also discussed in this chapter. To complete wettability study, static and dynamic contact angle measurement methods and influential factors are presented. Three wetting models for surface study are discussed.

Laser machining method to fabricate hydrophobic surface is presented in Chapter 3. In this chapter, the development of laser fabrication of hydrophobic surfaces is reviewed. Four micro structures are shown in this chapter. Laser-treated samples before coating and after coating are investigated. Contact angle measurement and analysis are presented. An OCA 15 contact angle instrument was used to determine their static contact angle and hysteresis.

In Chapter 4, the sandblasting method is discussed in detail. Two metallic materials including

A350 Gr Lf 2 carbon steel and 17-4 PH stainless steel are chosen to be sandblasted under different standoff distances. This chapter also discusses applications, process and parameters of sandblasting fabrication. The sandblasted samples are divided into coating group and uncoated group. Static contact angle and hysteresis are used to represent their wettability. The wettability differences between the two materials are investigated.

Laser machining and sandblasting in hydrophobic surface fabrication are compared in Chapter 5. The SEM results of top view and side view of the samples are used to show the topography difference. The sandblasted samples are compared with laser-machined samples: pillar and varied pillar. The wettability difference, in terms of static contact angle and hysteresis, is analyzed in this chapter.

Chapter 6 concludes the main results of the thesis and gives several suggestions for future work.

Chapter 2

Literature Review

2.0 Introduction

This chapter presents an overview of basic knowledge on hydrophobic surface and wetting characteristics. Section 2.1 introduces some applications of hydrophobic surfaces including ice-proof, self-cleaning and drag reduction. Several hydrophobic surface fabrication methods are presented in Section 2.2 such as laser machining, sandblasting, electrospinning, electrochemical deposition etc. Then, static and dynamic contact angle measurement methods are introduced in Section 2.3. For dynamic contact angle measurement, three main methods are introduced: sessile drop method, Wilhelmy method and captive bubble method. In Section 2.4, some factors that may affect static contact angle and hysteresis are presented. Three wetting models are introduced in Section 2.5 including Young model, Wenzel model and Cassie-Baxter model. Young model and Cassie-Baxter model are applied in Chapter 3 to get calculated contact angles and compared with measured values.

2.1 Applications of Hydrophobic Surfaces

Hydrophobic surfaces on metal substrates are widely used in industries and daily life because they have some special properties. Currently, hydrophobic surfaces have already been applied in ice-covering-proof, self-cleaning, drag reduction in fluid flow and so on.

Ice-covering-proof

Icing occurs in low temperature which can result in ice adhering to surfaces. Some outdoor setups have the requirement of ice-covering-proof, e.g., outdoor aerials at house roofs, solar panel and power lines. Hydrophobic surfaces can efficiently reduce snow accumulation on

surface of outdoor setup and therefore relieve interference from snow. Power lines can be sheared off due to ice and snow accumulation. When airplane flies through a low temperature zone, the accumulated ice on its surface is also a security threat [1]. Ice and snow accumulation can also decrease the efficiency of wind turbines operating in harsh environment like the polar regions [2]. Cao et al. [3] proved that hydrophobic surfaces can prevent ice formation in both lab condition as shown in Figure 2.1 and outdoor condition.

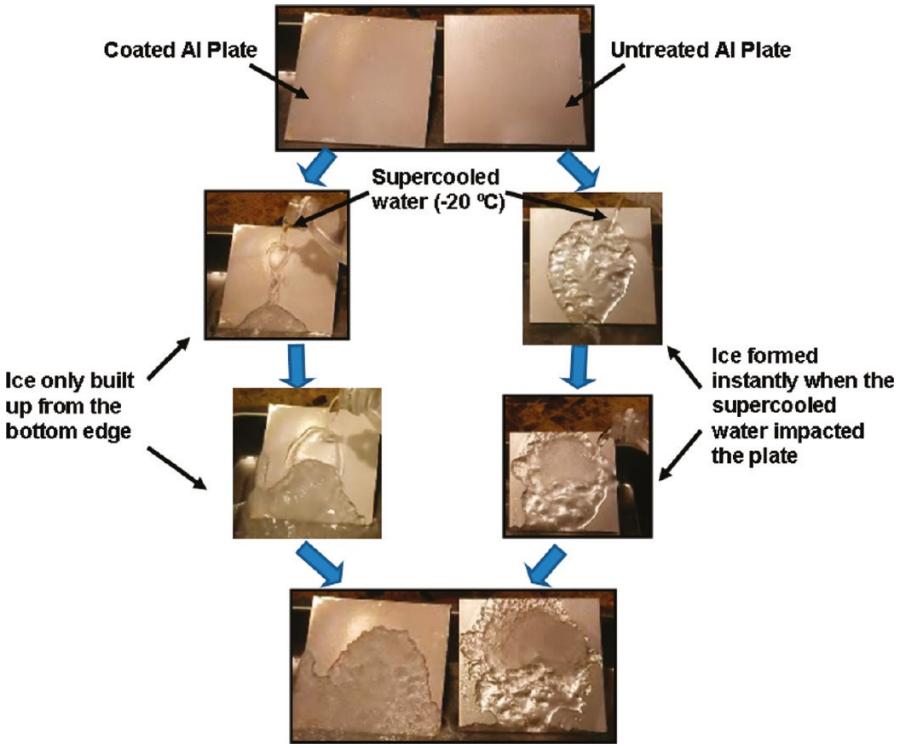

Figure 2.1 Ice Formation Tests under Lab Conditions [3]

The superhydrophobic surfaces are prepared from nanoparticle-polymer composites. From their experiments, they found that anti-icing efficiency is dependent on the size of nanoparticles. When the size of nanoparticles is small enough, ice will not form on the surfaces. In this case, 20 nm and 50 nm particles shows good anti-icing capability. The critical point is 50 nm because icing probability will increase when the size larger than 50 nm as shown in Figure 2.2.

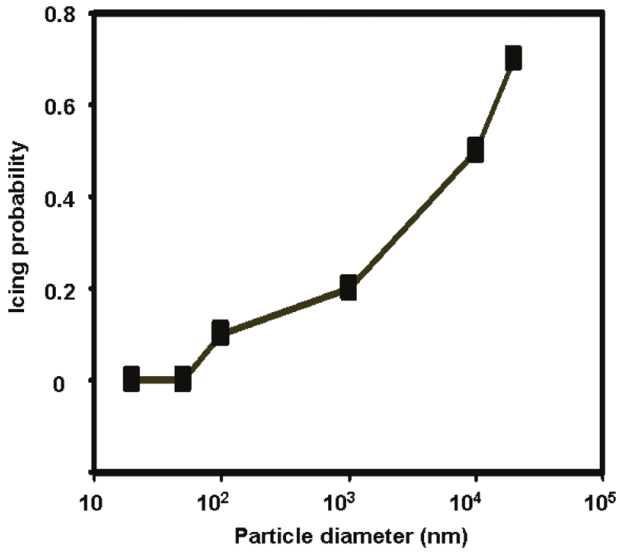

Figure 2.2 Icing Probability Changes with Different Particle Sizes [3]

Self-cleaning

Self-cleaning property is common in nature. For example, lotus leaf surfaces with a hierarchical structure and hydrophobic surface chemistry can provide high contact angles (>150°) and low hysteresis. This property can make water droplets easily roll off, pick up contaminants, and clean the path along [4]. This ability is called self-cleaning, also known as the lotus effect. Lu et al. [5] developed a kind of hydrophobic paint that can be applied on various substrates. Different abrasion tests including knife-scratch and sandpaper abrasion have been done and the surface durability was proved to be robust. Lab experiments have been done to show the self-cleaning ability of the new hydrophobic paint as shown in Figure 2.3.

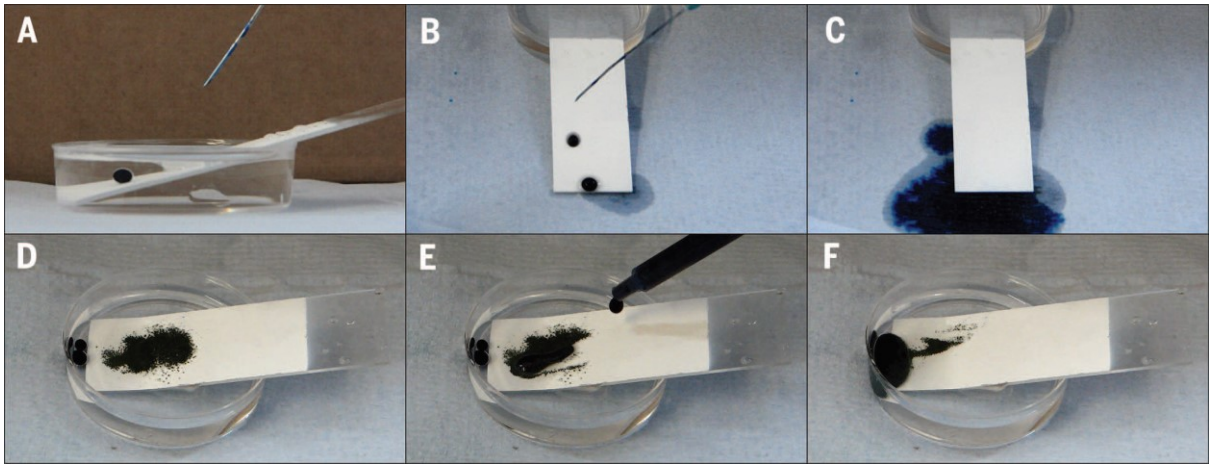

Figure 2.3 Hydrophobic Paint that Utilizes Self-cleaning Ability to Remove Oil Contaminations on Surfaces [5]

Drag reduction in fluid

Drag reduction can be achieved by using micro structure and coating. This property has a wide range of applications such as oil transportation. Microstructure can trap air and reduce the contact area between fluid and metal surface. The air layer is a kind of lubricating part that can lead to water slip which is related to drag reduction. The role of coating on surface is to reduce surface energy which can help to achieve a higher contact angle. Nowadays, many coating methods have been combined with micro or nanostructures on metal surfaces. During liquid transportation, skin friction can prevent fluid flow and increase pump power cost. Hydrophobic surfaces applied to microfluidic device or pipelines can reduce the pressure loss effectively. Tian et al. [6] found superhydrophobic surface can reach a drag reduction benefit of up to 10 %. By comparing with hydrophilic plate in water channel, the suppression of coherent structure burst on superhydrophobic plate was found to achieve drag reduction. Besides suppression of coherent structure burst, effective slip lengths were a key factor that can help to achieve drag reduction. Truesdell group [7] found that coating and longitudinal grooves could be beneficial to increase slip lengths.

2.2 Summary of Hydrophobic Surface Fabrication Methods

The preparation of superhydrophobic surfaces usually has three ways: the first way is to create microscale or nanoscale structure, and even multi-level composite structures. The second way is to create a hydrophobic thin film. The third way is combining the first two ways together: cover the textured surface with low surface energy coating and make sure the cover will not destroy the structures underneath. Some common methods that can be used to fabricate hydrophobic surface are summarized below.

Laser machining method

Laser machining method is a physical process. Via high energy laser beam, regular microscale structure can be obtained under high artificial control. Various structures have been developed including grooves, pillars and so on. Laser machining method has been widely used on hydrophobic surface fabrication because of its increased versatility that allows it to be used on almost all metals. With laser irradiation, complex shapes and structures can be achieved with high-accuracy by adjusting laser exposure parameters (energy, scanning speed, pulse duration, wavelength, polarization, etc.) while accounting for different material characteristics (thermal conductivity, band gap, etc.) [8]. In recent years, laser surface treatment was found to enhance the mechanical properties of the surface [9–10]. Tang et al. [11] created a superhydrophobic surface on aluminum alloy with a facile laser marking approach. The irregular protrusions can help to achieve high contact angle (155.1°), and the surface also showed self-cleaning ability. The laser-treated surface performed superior abrasion resistance and mechanical stability. Three steps of laser fabrication process are shown in Figure 2.4 in details.

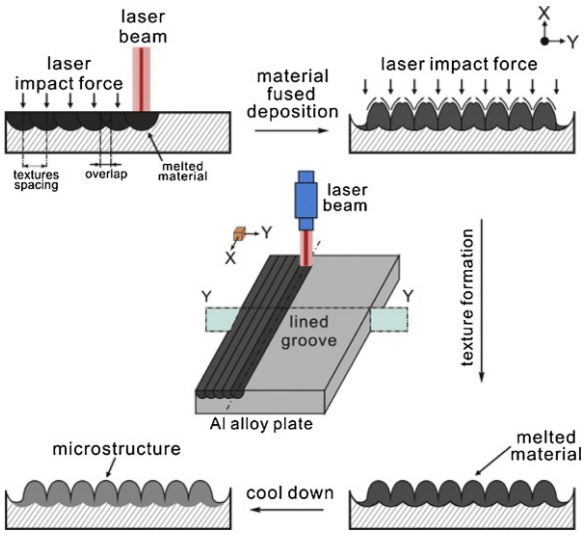

Figure 2.4 Three Steps to Use Laser Beam to Fabricate Hydrophobic Surface [11]

With a femtosecond laser, Martínez-Calderon et al. [12] developed hierarchical structures on a stainless steel alloy (AISI 304) surface at high pulse energy. Superhydrophobic ability was achieved by adjusting the pitch distance value, and the limit of the pitch distance value which can be transited from hydrophilicity to hydrophobicity was found. With pitch distance higher than 50μm, the water contact angle will be significantly reduced. The microstructure designs are shown in Figure 2.5.

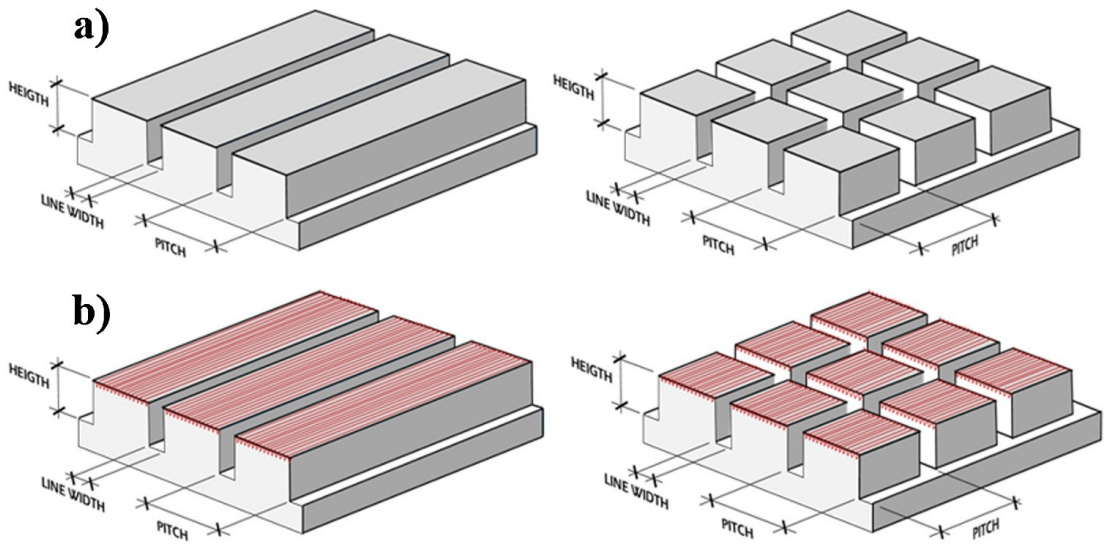

Figure 2.5 Microstructure Design on Target Surface, (b) Nanostructure Design on Top of Microstructures [12]

The relationship between laser fluence and water contact angle was found by Liang et al. [13] when applying femtosecond laser irradiation on 316L stainless steel. With higher laser fluence and scanning speeds, water contact angle can be increased from 127.2° to 142.5°.

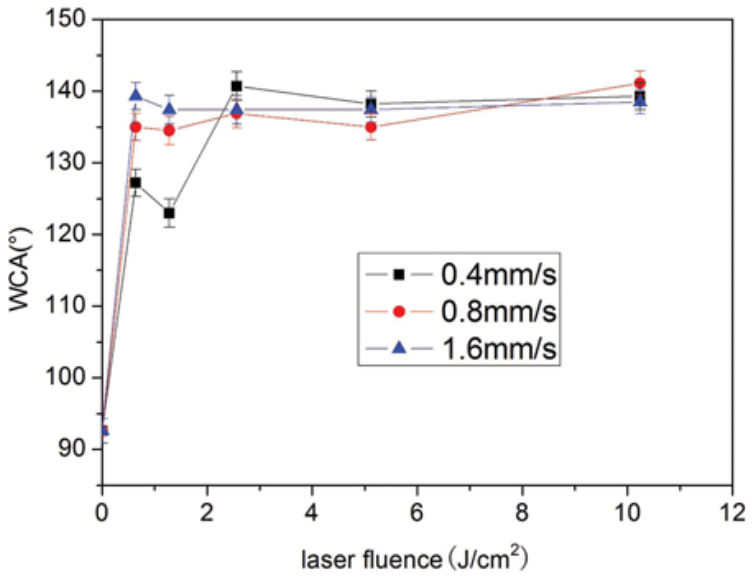

Figure 2.6 Water Contact Angle Changes with Different Levels of Laser Fluence [13]

Sandblasting method

Sandblasting method can be used in surface treatment in different ways. Sandblasting process can increase roughness of a target surface. By adjusting injecting pressure, standoff distance and blast media, different wetting abilities can be achieved. Proper roughness may lead to a more hydrophilic surface which can be beneficial to coating application. With higher roughness created, the Wenzel state will transit to Cassie state and the surface can be turned hydrophobic.

The effects of abrasive particle size, kinetic energy of the abrasive particles and standoff distance on roughness have been investigated by many researchers. Slatineanu et al. [14-15] proved that the surface roughness parameters increase with the increase of the abrasive dimensions and of the kinetic energy of the abrasive particles. Different roughness parameters are shown in Figure 2.7. Meanwhile, they found that higher standoff distance can decrease roughness. They also provided an empirical model to estimate roughness values.

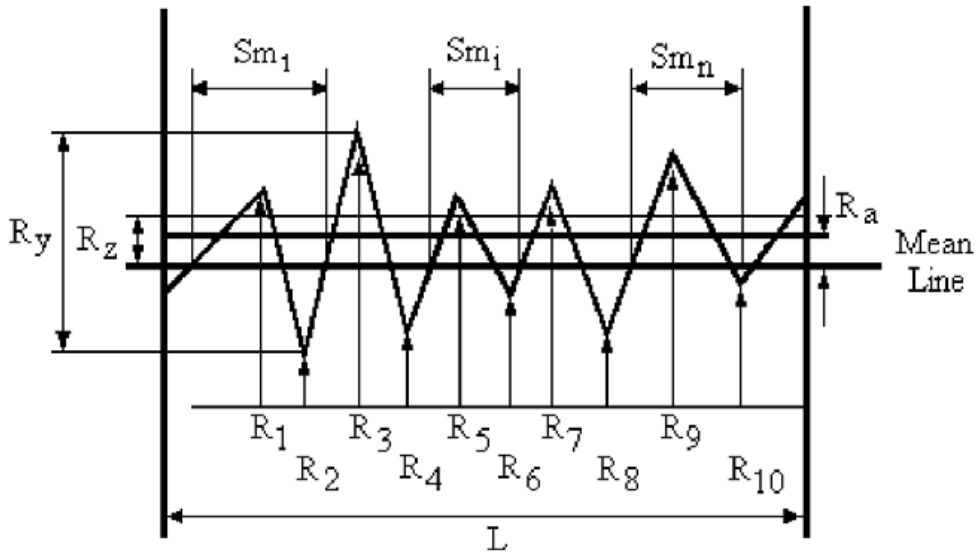

Figure 2.7 Roughness Parameters Illustration [14]

Considering rust protection, stainless steel was applied as a substrate by Beckford and Zhou [16] to determine the topography resulting from these surface modifications. Scanning electron microscopy and surface profilometry was used to analyze the change of the topography. The wetting properties of these surfaces were characterized by water contact angle measurement and the maximum water contact angle found was 163°. The results illustrated that both sandblasting and coating can affect the contact angle. Sandblasting can affect contact angles by increasing the surface roughness and coating can reduce the surface energy. From Figure 2.8 and Figure 2.9, one can see that the contact angles of the samples are higher than untreated ones after being sandblasted and coated. The reason is that the samples' roughness is increased and surface energy is decreased after sandblasting and coating.

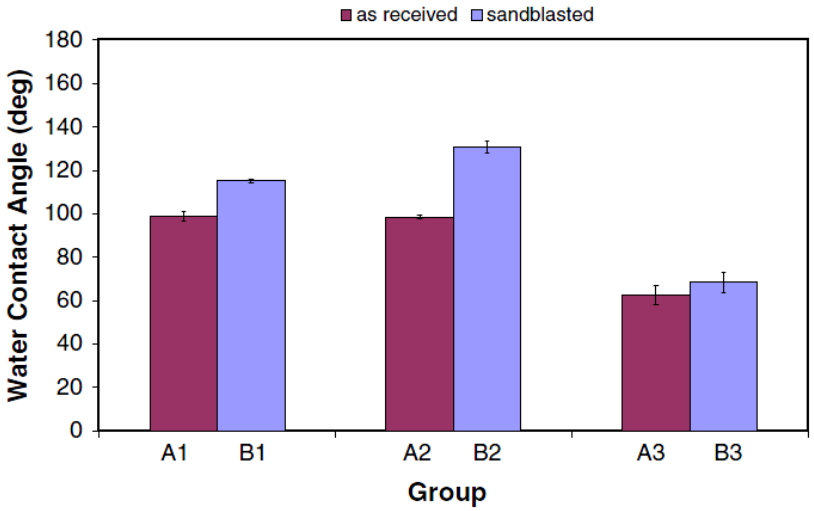

Figure 2.8 Water Contact Angle Comparison Between Smooth Samples and Sandblasted Samples Before Coating [16]

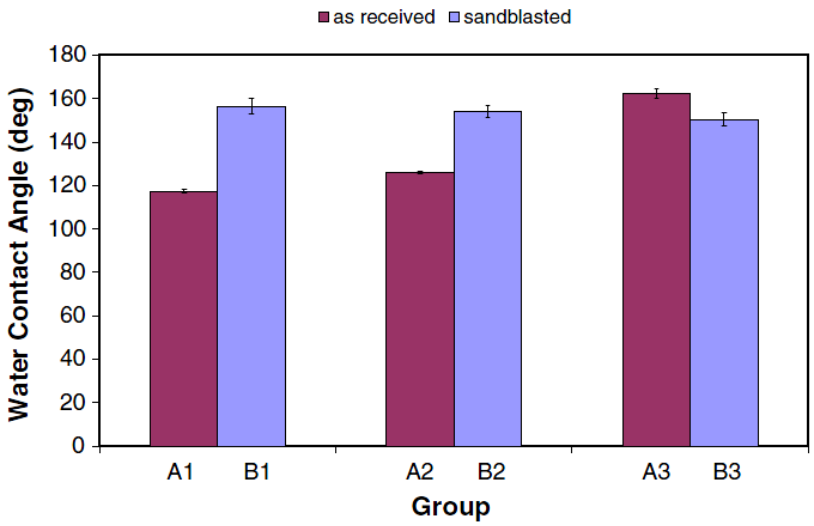

Figure 2.9 Water Contact Angle Comparison Between Smooth Samples and Sandblasted Samples After Coating [16]

Cabello group [17] combined sandblasting with acid etching method together on galvanized steel. Microscale and submicron structures were observed and proved to have contributes to surface water repellency. Microscale roughness plays an important role in wettability performance before Ra equals 3.5μm. Above 3.5μm roughness, nanoscale roughness seems more prominent than roughness in microscale. Sandblasted group shows better dynamic contact angle performance than non-sandblasted group.

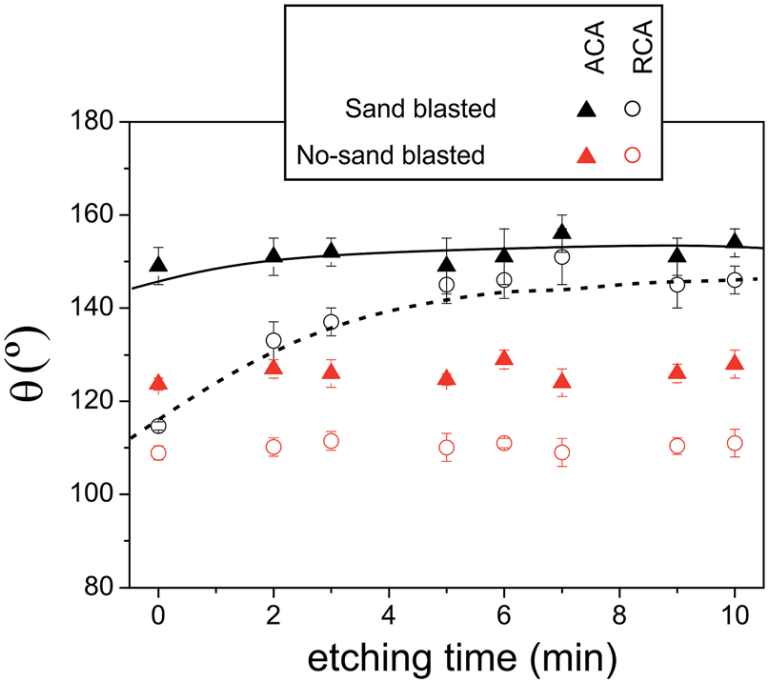

Figure 2.10 Dynamic Contact Angle Comparison Between Non-Sandblasted Samples and Sandblasted Samples [17]

WEDM method

Wire electrical discharge machining (WEDM) is mainly used to make channel and pillar on metal surface. Micro electrical discharge machining (micro-EDM) is a branch of EDM, which is usually used to fabricate microscale components. The principle of Micro-EDM is to utilize low discharge thermoelectric energies between the workpiece and an electrode (non-contact) to remove redundant material from target surface through the process of melting and vaporization [18]. One-step method to fabricate dual-scale structures was applied on metal surface by Bae et al [19]. With wire electrical discharge machining, sinusoidal pattern was made on Al 7075 alloy surface and exhibits good water repellency ability (water contact angle=156°, hysteresis≈3°) The following Figure 2.11 shows the WEDM process during operating on metallic surfaces.

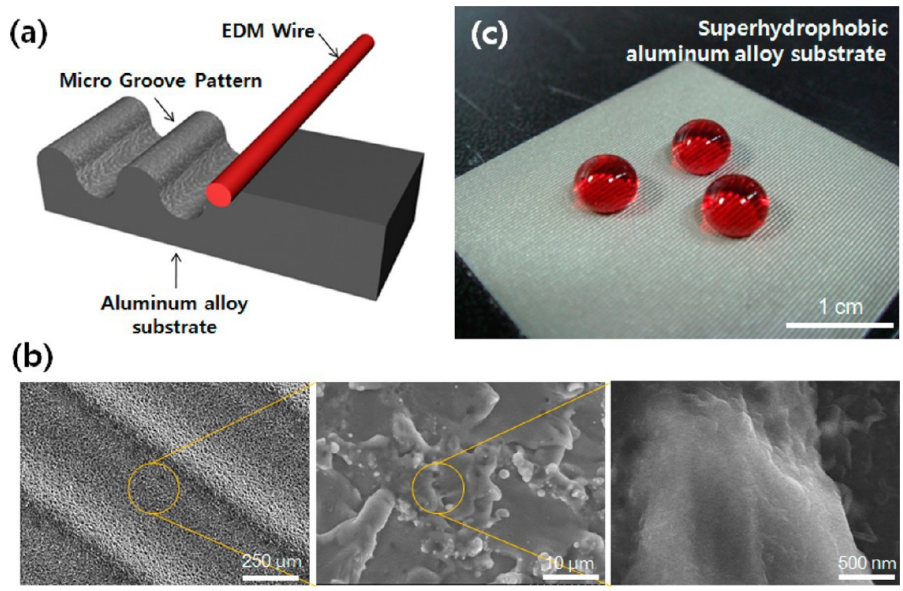

Figure 2.11 (a) Schematic Illustration of the WEDM Process, (b) SEM Images of WEDM-Treated Surface on Al 7075 Alloy Surface, and (c) Water Droplets on the WEDM-treated Surface [19]

Weisensee et al [20] developed "micro-mushroom" structures on steel surface by using micro electrical discharge machining (MEDM). The liquid repellency of water, oil and isopropanol were tested and proved the treated surfaces by MEDM owns both hydrophobic and oleophobic properties. For the repellence of oil and isopropanol, closer spacing and stronger "micro-mushroom" features are important to provide enough support from underneath. For water contact angle tests, post-like micro-mushroom geometries are better than other samples. Micro-mushroom with different geometries are shown as below.

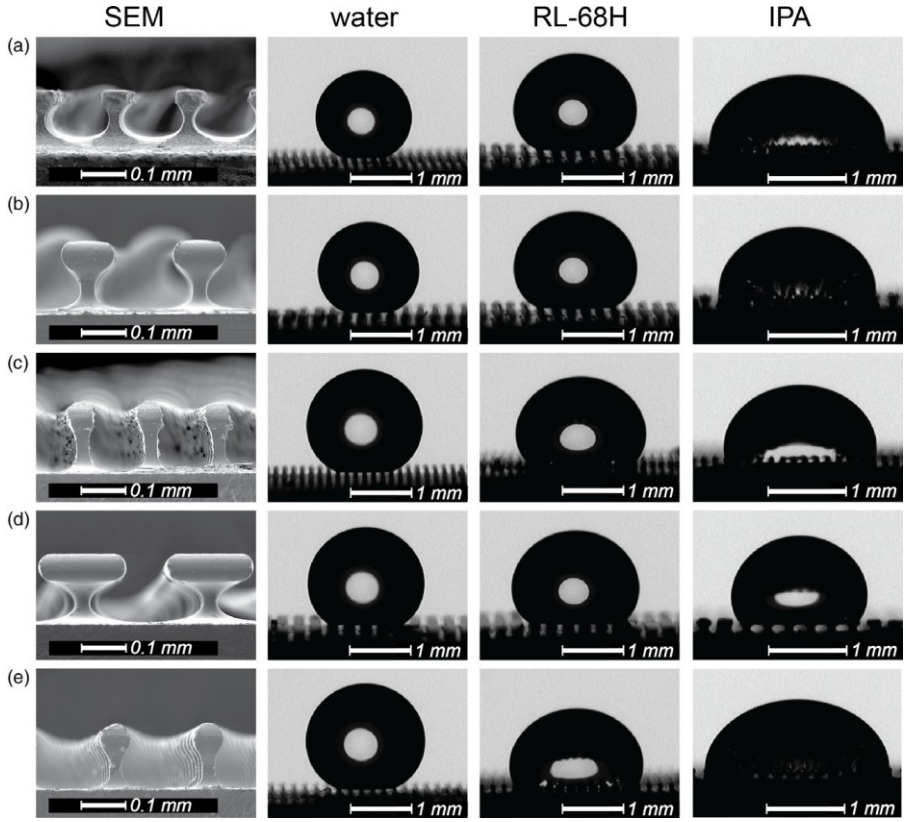

Figure 2.12 Surfaces with Different Micro-Mushroom Geometries. Contact Angle Tests for Water, Oil and Isopropanol are shown from left to right. Droplets Volume≈5 µl [20]

Electrospinning

Electrospinning is a process of changing polymer solution to fiber (3nm~5µm) under high voltage electric field. The hydrophobic thin film from electrospinning owns many advantages such as high uniformity, porosity and specific surface area. It is an effective method for mass production of nanofibers. The morphology of the nanofibers is mainly affected by the polymer properties (relative molecular weight, molecular structure, solution concentration), electrospinning conditions (applied voltage, standoff distance between nozzle and collecting plate) and environmental conditions during reaction (temperature, humidity and airflow rate). By applying electrospinning method, nanofibers with hydrophobic polyvinyl butyral (PVB) shell were made by Sun et al [21]. Ethanol was used as solvent. Better nanofibers were obtained under higher PVB concentration. The nanofibers' stability and repeatability were tested under

room temperature. The nanofibers show good thermoregulating capability in environmental conditions.

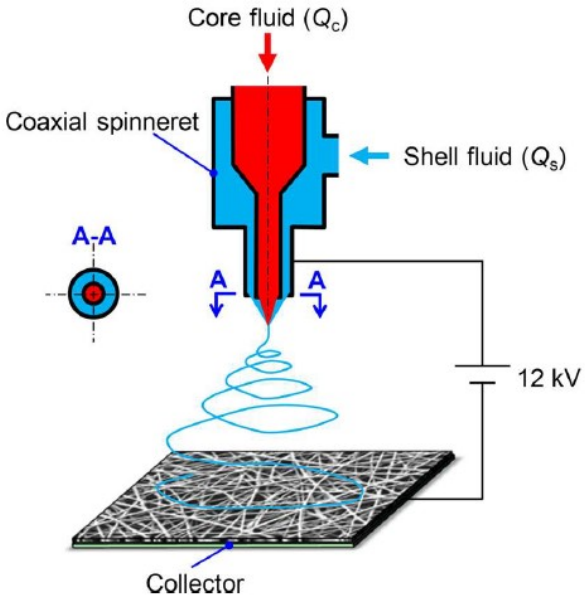

Figure 2.13 Schematic Illustration of Electrospinning Method Application Process [21]

Miyauchi et al [22] achieved superhydrophobicity on fiber mats by applying Polystyrene (PS) microfibers. By changing solvent compositions, structures in micro- and nanoscale can be optimized. By adjusting the solvent composition, the optimal combinations were found as THF/DMF ratio of 1/3. The water contact angle was improved from 143.8° to 159.5°.

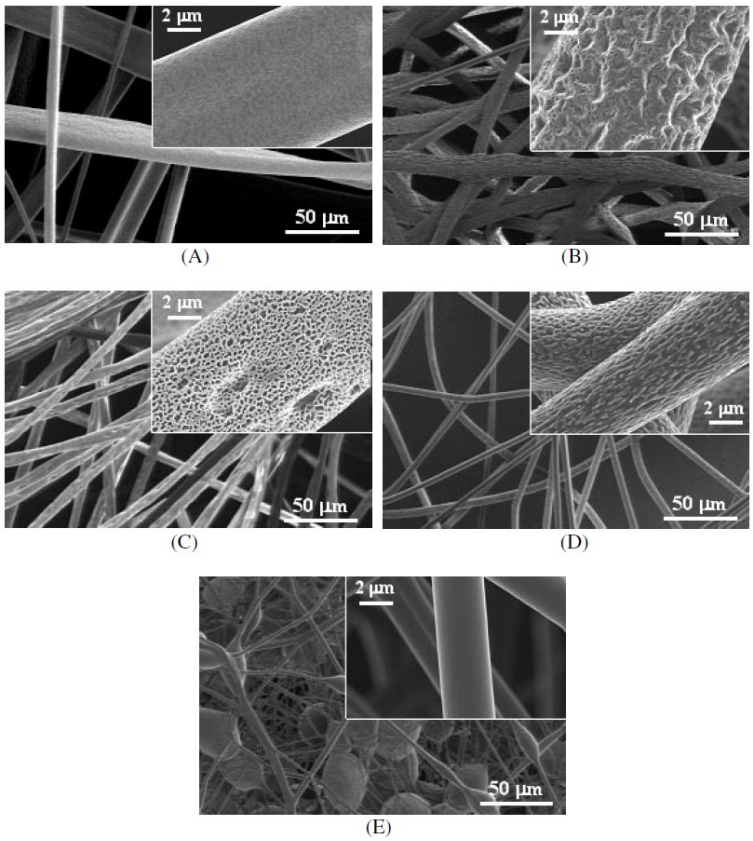

Figure 2.14 The Electrospinning Treated Surfaces from Different Operating Combinations. Weight Ratios of Tetrahydrofuran (THF)/ N-dimethylformamide (DMF) in Solvent [22]

Lay-by-Layer (LbL) assembly method

Lay-by-Layer (LbL) is also called alternating deposition. Its greatest advantage is to avoid nanoscale or microscale structures destroyed by the thickness of modified coating. Its principle is the use of the forces among static electricity, oxygen bond, and coordinate bond to generate thin film at molecular level. Han et al [23] created a hydrophobic surface by poly (allylamine hydrochloride) and ZrO_2 nanoparticles. By applying layer-by-layer (LBL) deposition, chemical and mechanical durability of the surface were demonstrated to be good. Heat-induced cross-linking of the film was proved to improve chemical stability of the film. Higher number of deposition cycles can increase water contact angle.

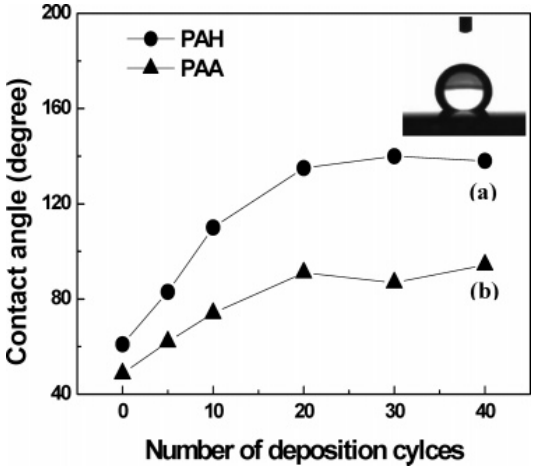

Figure 2.15 Contact Angle Measurements on the Deposited Surface from Lay-by-Layer (LbL) Assembly Method [23]

Zhao et al [24] developed a hydrophobic surface by applying silica nanoparticles on cotton fibers. They found that the wettability was influenced by the number of layers. Although superhydrophobicity goal was achieved, the samples' hysteresis is higher than 45° when the number of layers is less than 3. With more accumulated layers, the hysteresis was reduced to 10° which is much lower than 45°. Silica nanoparticles was also used in Li's research group [25]. The difference is the substrate they adopted is glass. As the difference in substrate, their hysteresis is less than 1°.

Template printing

The template printing method is to fabricate microstructures by controlling the morphology and the size of the template. With mechanical squeezing, a microscale structure will be formed on the target substrates. By applying template printing method, Qu et al [26] obtained polydimethylsiloxane (PDMS) superhydrophobic surface. Its water contact angle is as high as 173°. The two-step replicating method they used started with using fresh fish skin as their template, then applying Polyvinyl alcohol (PVA) on the skin surface. The procedure is shown in detail.

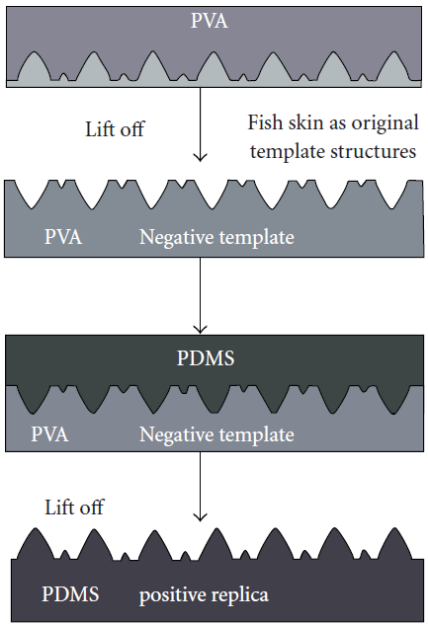

Figure 2.16 Illustration of the Fish Surface Structure Duplication Process [26]

Karaman et al [27] mimicked rose petal on two-layer polymer sheet which consists a supporting layer and a functional layer. The contact angle of the treated surface is 152±3°. The treated surface duplicated the "petal effect" successfully which means high contact angle with high hysteresis. Top droplet shows superhydrophobicity but cannot roll off even reverse the sample. Locust wings were mimicked by Gang et al [28] and the contact angle of the polymer film they created is 144° compared with 152° of locust wings' surface. The wettability was caused by surface energy of substrate and multi-scale structures.

Electrochemical deposition

Electrochemical deposition of films can be applied to create superhydrophobic surfaces. Roughness value can be increased by electroplating at underpotential or diffusion-limited conditions. Yu et al [29] combined electrochemical deposition with chemical deposition to fabricate superhydrophobic Ni–P film. The water contact angle of the surface is 155.5° and the hysteresis is lower than 2°. They found the solution temperature can affect film's morphology and further increase chemical deposition.

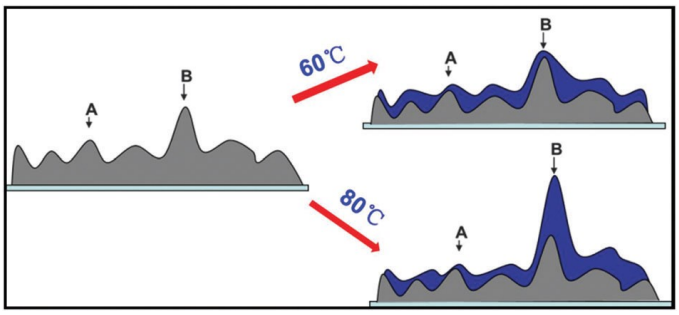

Figure 2.17 The Schematic Illustration of the Films Growth Mechanism Under Different Temperatures [29]

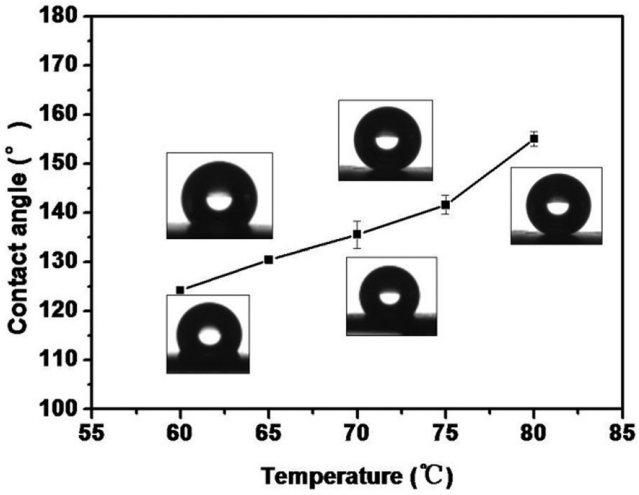

Figure 2.18 The Contact Angle Changes with Increasing Temperature [29]

Hang et al [30] found the size of micro-nanoscale cones can affect the contact angle of the surface from electrochemical deposition. The span of contact angle is from 87° to 154°. Lager size of cones is beneficial to achieve higher water contact angle. He and Wang [31] applied electrochemical deposition on zinc substrate. They found that the aspect ratios of ZnO nanorods and the density of hydroxyls can affect contact angle of the surface. More hydroxyls can decrease contact angle. The best contact angle they obtained is as high as 167°. Ishizaki et al [32] used magnesium alloy AZ31 as substrate and applied chemical vapor deposition on its surface. The anti-corrosion mechanism of the treated surface from electrochemical deposition was also investigated. They found the trapped air among the structures can reduce the actual area in contact with top liquid.

Sol-gel method

Sol-gel method adopts highly chemically active compounds as precursor for hydrolysis. After obtaining the sol, condensation reaction will occur in hydrolysis products and form a stable gel. After removing solvent from the gel, lots of coves in nanoscale will appear on the substrates. These nanoscale structures can change the surface to be superhydrophobic. Sol-gel method can be applied on non-metals such as glass and mass production can be carried out with low cost.

Gurav et al [33] adopted the sol-gel method to obtain a transparent superhydrophobic surface under room temperature. Mixing tetramethoxysilane (TMOS), methanol and water with the ratio of 1:12.36:4.25 for 30 min to obtain the coating sol. Distributing the coating sol equally on glass substrate then heat-treated under 80 °C to get a thin film. Using hexamethyldisiloxane (HMDSO) and hexamethyldisilazane (HMDZ) to modify the films to achieve superhydrophobic surface with dense and porous properties. Nadargi et al [34] applied silica films on glass and obtained hydrophobic surface. They obtained optically transparent surface and the contact angle is around 120°. Deposition time in solution can affect the uniform of the thin film on substrate. When the deposition time in solution is longer than 20min, the thin hydrophobic film can be uniform. Mahadik et al [35] also obtained optically transparent superhydrophobic surface on glass substrates. The water static contact angle is as high as 167°±1° and the sliding angle is as low as 2°±1°.

Figure 2.19 The Optically Transparent Superhydrophobic Glass Surface from Sol-gel Method [35]

Melt coagulation method

The melt coagulation method is to cover the substrate by a specific chemical compound. By using heat treatment, phase change will occur in the chemical compound and structures in nanoscale will be formed on the surface. Minami et al [36] developed a superhydrophobic surface with Alkylketene dimer (AKD: a kind of wax), the water contact angle is as high as 174°. Melt the wax sample on glass substrate and cover it uniformly. The melted wax sample solidified under room temperature. An empirical general rule for the wax sample was found that a metastable crystalline phase should form during solidification process. Then the superhydrophobic surfaces form spontaneously from a metastable to a stable crystalline form. AKD is widely used in paper industry to change paper to be hydrophobic. The experiments were designed for paper industry by Wang et al [37]. They found AKD barriers can be breached by alcohols. Shin et al [38] tested evaporating characteristics on AKD surfaces. They found hydrophobic property can shorten the pinning time and extend the total evaporation time.

Coating method

Coating technique can be used to create hydrophobic surface. It is an effective way to achieve drag reduction (DR) and has a long history of application with pipelines in oil and gas industry. Initially it was mainly used in natural gas transportation, with the earliest application by Tennessee Gas Pipeline Co. in 1955. Compared with natural gas, oil especially crude oil has higher viscosity. Moreover, impurities such as silt and sands will result in worse corrosion and abrasion. Based on non-Newtonian fluid research [39], erosion–corrosion resistance tests [40] and thermal conductivity [41], an ocean of internal linings and coatings have been developed in pipeline transportation.

After long-term experimental tests under dissimilar subsea conditions, industry and academia found that protective internal lining and coating can save a large amount of money based on the following four reasons:

(1) Improving flow efficiency [42] and saving pumping power costs.
(2) Anti-corrosion [43] and reducing periodic maintenance and repair expenses.
(3) Increasing pigging [44] and scraping efficiency and shortening shut-in period and improving thermal insulation performance [45] and saving electrical heating charge.

Based on the four advantages above, investment on coating can be paid back within a few years and can meanwhile create predictable economic benefits. The reason why drag reduction (DR) and cost saving can be achieved by coating technique is that pipeline inner roughness can be significantly modified with a much smoother coating cover [46-49]. Epoxy coating is widely used in pipeline transportation due to its outstanding adherence[50].

Transportation pipelines under deep sea need to cope with environmental exigencies. Firstly, pigging and scraping fee is much higher than that on land operation. In addition, if hydrate formation and wax deposition occur, the pipeline will be blocked up and even crack. Based on

these two reasons, industry makes excessive demands of improved epoxy coating to adapt to harsh environment. Good flow efficiency can flush the deposition and carry impurities. In order to improve flow efficiency, DR is considered as a function of Reynolds number, flow regime, viscosity and adhesion, and wettability of wall. The factors affecting drag reduction efficiency from coating are mainly divided into two parts: liquid properties and solid properties.

- **Liquid Properties** (Reynolds number, flow regime, viscosity)

Ou et al. [51] demonstrated that the combination of microscale roughness and hydrophobicity can result in DR in laminar flow. Further studies have been conducted by Daniello et al. [52] who measured the DR in turbulent flows, and maximum 50% DR was achieved which is higher than the 40% DR obtained in Ou's work. The interesting thing is no DR was observed in the laminar regime in Daniello's work. Their explanation about this phenomenon is the presence of a shear-free interface and also applicable in the slip velocities they observed. However, both of their experiments are based on materials with low surface energy, silicon wafer and polydimethylsiloxane respectively. Moreover, they just roughly classified the flow regimes as laminar flow and turbulent flows.

Different flow regime can lead to different drag reduction efficiencies. Flow regime is categorized by liquid viscosity, water cut, flow rate, pipe size and wall properties. From Figure 2.20, the liquid contacting the pipeline internal surface is mainly water rather than oil because the water ratio reaches an inversion point and shape as a continuous phase (oil in water emulsion will be inverse to water in oil emulsion) [53, 54]. In oil industry, water cut is usually higher than 70%, so the four patterns in Figure 2.20 are the most common in oil transportation (ignore gas). Thus, there is no need to make amphiphobic or oleophobic coating, hydrophobic coating is enough considering common flow patterns in oil transportation pipeline.

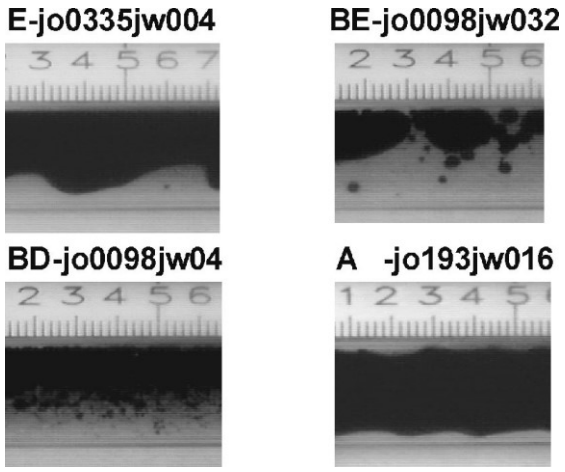

Figure 2.20 Four Typical Flow Patterns in Horizontal Pipeline [54]

- **Solid Properties** (Roughness, wettability)

Compared with common pipes with oversized roughness, proper roughness can trap air and thus reduce the contact area between passing fluid and metallic surface[55]. Proper roughness contributes to higher drag reduction than a smooth surface at comparable conditions. Petrie et al. [56] drew the conclusion based on their experimental results from a study of surface roughness effects on polymer drag reduction in a zero pressure gradient flat-plate turbulent boundary layer. However, roughness is not the only influential factor. The material of the tube wall can strongly affect drag reduction in liquid – liquid flow. Controlled variable including mixture velocities and flow volume fractions, material's properties such as wettability may have greater effects on pressure gradients than that of the wall roughness [57]. Contrary to most traditional opinion: fine micro structures on a superhydrophobic surface can usually reduce liquid-solid contact area and adhesion to water droplet, Teisala et al. [58] proved that this principle does not apply to a rose petal surface with high adhesive and superhydrophobic ability. To achieve drag reduction, hydrophobicity is just a prerequisite but not sufficient. Just like a water droplet on lotus leaf, it can slide easily because the rolling-off angle is very small (3 ± 0.6°) [59], which is called self-cleaning effect. But the same droplet won't slide easily on rose petal, as the petal's adhesion is so strong .

2.3 Static and Dynamic Contact Angle Measurement Methods

Wettability is one of the most important properties of solid surface and usually represented by static and dynamic contact angle. It is determined by surface energy and surface structure.

Static Contact Angle

Static contact angle is measured when the contact angle becomes stable and not changed depending on time. During contact angle measurement, after dropping a pending droplet, generally 10 seconds to 1 minute should be waited until the droplet completely pinned on target surface.

- Contact angle=0° complete wetting (clean gold [60])
- 0°<contact angle<90° partial wetting
- 90°<contact angle<180° nonwetting
- Contact angle=180° complete nonwetting

With respect to water droplet, the terms “hydrophilic” and “hydrophobic” are often used.

- Contact angle<90° hydrophilic
- 90°<Contact angle<150° hydrophobic
- Contact angle≥150° & hysteresis<10° superhydrophobic

Dynamic Contact Angle

There is only one constant value for contact angle on a flat, homogeneous ideal surface. For a surface in practice, contact angle will change between two values because of heterogeneity and roughness. The maximum value is the advancing angle and the minimum value is the receding angle. There are several ways to measure dynamic contact angle including: sessile drop method, Wilhelmy method and captive bubble method.

(1) Sessile drop method

The advancing and receding angles are dynamic contact angles related to a moving drop. One way to measure these dynamic angles is to add or remove liquid to or from the drop, e.g. by leaving the tip of the needle inside the drop, as shown in Figure 2.21. If a small amount of liquid is added to a drop, the contact line will still be pinned, but the contact angle will increase. Similarly, if we remove a small amount of liquid from a drop, the contact line will still be pinned, and the contact angle will decrease. The advancing and receding angles are defined as the contact angles measured just before the contact line breaks or is shifted. Therefore, a drop placed on a surface has a range of dynamic contact angles from the so-called advancing (maximal) contact angle, θ_A, to the so-called receding (minimal) contact angle, θ_R.

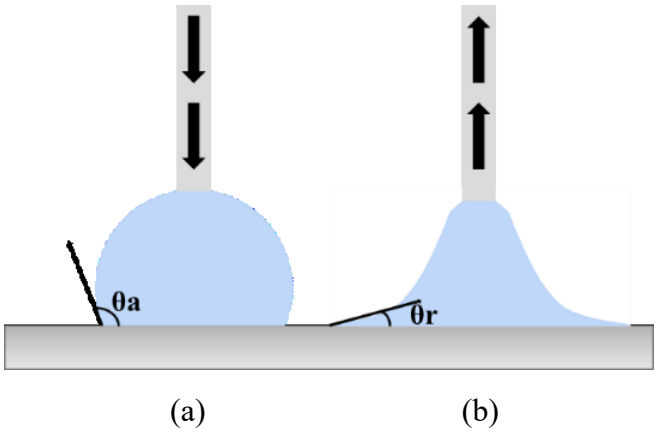

Figure 2.21 Advancing (a) and Receding (b) Contact Angles

(2) Wilhelmy method

The Wilhelmy method is widely used in dynamic contact angle measurement. The requirement for applying this method is to make sure that the two sides of the sample surface should be same in properties. By immersing in and pulling up solid sample from a liquid, the contact angle can be measured. Románszki et al [61] measured dynamic contact angle on alloy samples by adopting Wilhelmy method. Three different samples were prepared for dynamic contact angle measurement. After the experiments, they found the disadvantage of Wilhelmy method

is that the experimental error became larger when measuring both high and low-level contact angle values.

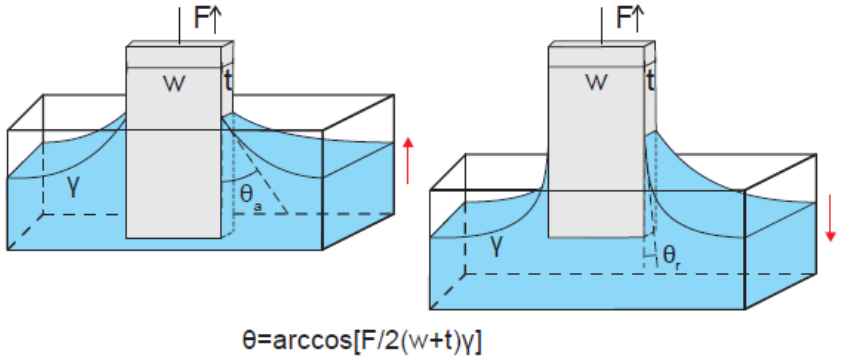

Figure 2.22 Schematic Illustration of Wilhelmy Method Measurement [61]

(3) Captive bubble method

The solid surface on the liquid surface should be reversed first then inserting a bubble by micro syringe. Contact angle can be only measured until the bubble is stable. Adding or reducing air from the bubble, repeat operation until same values obtained from consecutive measurements [62].

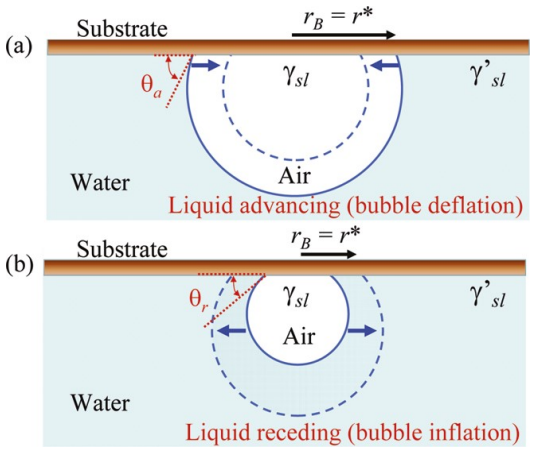

Figure 2.23 Schematic Process of (a)Advancing Contact Angle and (b)Receding Contact Angle [62]

Szyszka [63] applied the captive bubble method to measure the contact angle of copper-bearing shales. After trying active surfactants, he found the wettability of copper-bearing shale was changed. The application of frothers can decrease the stability of thin film.

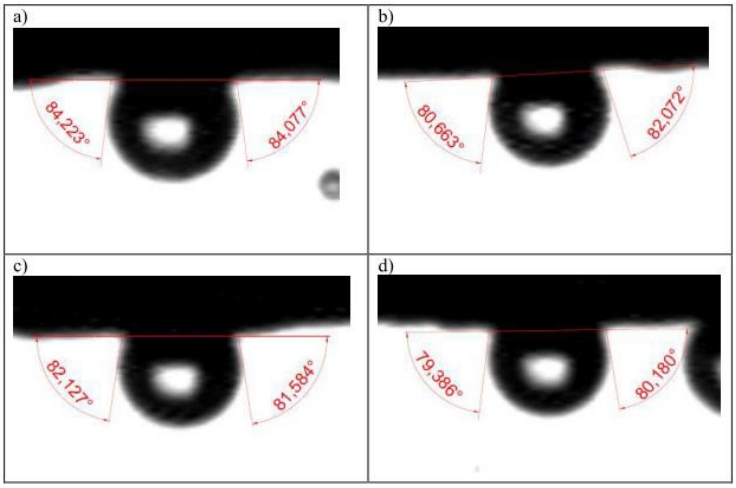

Figure 2.24 Images of Contact Angle Measurements by Using Captive Bubble Method [63]

2.4 Factors Affecting Contact Angle

Sessile contact angle and hysteresis are two main measures to evaluate wettability characterization. Previous research showed that the sessile contact angle and hysteresis measurements are affected by several factors including salinity, drop size, coating, micro-structure, temperature and pressure. Salinity factor can increase both sessile contact angle and hysteresis which were investigated by many researchers. Jong-Won et al. [64] used two independent approaches to do the same tests and obtained consistent results. They found that the contact angle linearly increased with ionic strength when NaCl increased from 0 to 5.0 M. Similar results also showed that salinity can increase static contact angle of the air-water-silica system. Sghaier et al. [65] also showed that contact angles increase with ionic strength. At atmospheric pressure and 20 °C, contact angles of their targeted surface increased from 40° to 55° when the ionic strength was increased from 0 to 4.5 M NaCl. Saraji et al. [66] conducted

their experiment at 80°C. According to their results, there should be a positive correlation between salinity and hysteresis. Significant rise in hysteresis was observed from 6° to 22° with an increase in the ionic strength from 0.2 to 5 M.

Besides salinity, drop size may also affect wettability characterization, because gravity may distort the shape of the drop slightly. Extrand and Moon [67] examined a large range of drop sizes, varying from 1 to 2000 μL. They verified that for a large drop (>1000–2000 μL), the shape is surely distorted and influenced by gravity. To minimize this impact, the small volume regime (less than 10 μL) is frequently used in contact angle measurement.

Moreover, applying coating with low surface energy can significantly change contact angle and hysteresis. Artus et al. [68] applied silicone nanofilament coating with low surface energy and achieved superhydrophobicity on various substrates. They obtained superhydrophobic properties of a surface, including low surface energy and proper roughness, in a single fabrication step. Microscale structure from laser machining plays an important role in contact angle and hysteresis as well. The most important parameters for hydrophobic structures are the height of the structures and the spacing between them [69]. Bhushan and Jung proved that air pocket formation probability tends to vary inversely with spacing between bumps [70]. Effective air pockets are controlled by many factors. Smaller bump spacing usually contributes to better formation of air pockets. By analyzing surface roughness, adhesion and friction data for both hydrophobic and hydrophilic surfaces, they concluded that the combination of low surface energy material and proper roughness is the key for high hydrophobicity. Temperature and pressure can also affect contact angle. Sarmadivaleh et al [71] found contact angle will be higher with increasing pressure and temperature. They tested water-CO_2 contact angle on quartz surface. The possible reason is under high temperature and pressure, the CO_2 content will be decreased.

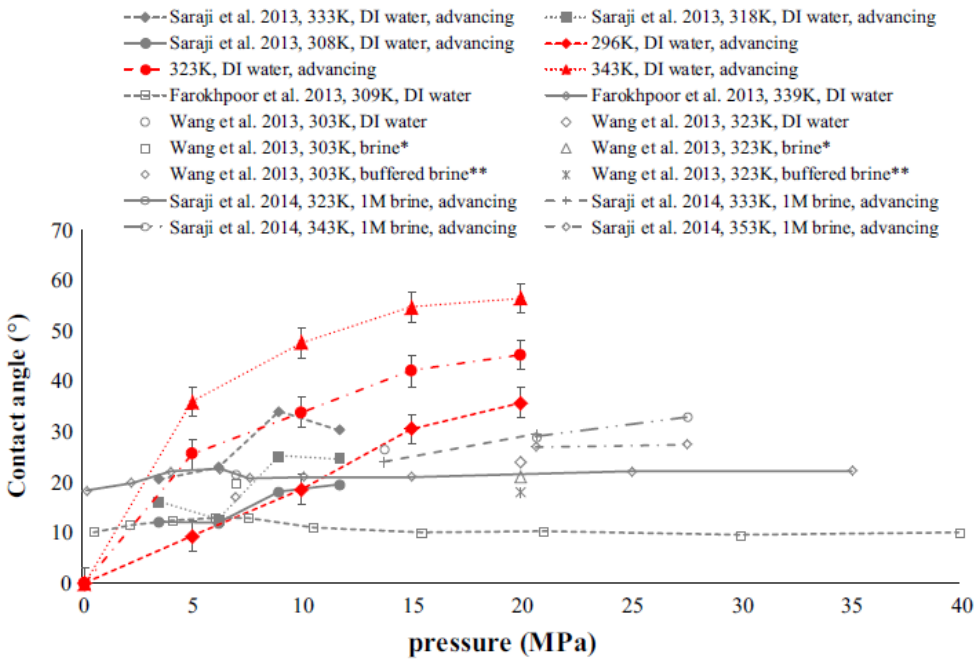

Figure 2.25 Contact Angle Trends with Pressure Under Different Temperatures [61]

2.5 Theories about Static Contact Angle and Hysteresis

2.5.1 Young's model

For a homogeneous, stable and flat ideal surface, Young [72] considered the contact angle decided by interfacial tension between solid-liquid γ_{SL}, solid-vapor interface γ_{SV} and liquid-vapor interface γ_{LV}. The contact angle of a droplet on a surface indicates the wettability of the surface. This can be found by considering the interaction between the solid (S), liquid (L), and gas (V) phases of a system interacting with one another due to surface tension, as shown in Figure 2.26. The angle between the solid-liquid interface and the liquid-vapor interface is the contact angle Eq. (2.1). Young's angle is simply the contact angle between a droplet and a smooth surface as shown in Figure 2.26 (a).

$$\cos\theta_Y = \frac{\gamma_{SV} - \gamma_{SL}}{\gamma_{VL}} \tag{2.1}$$

There exist two types of contact angle measurement that are useful when trying to verify if the observed contact angle is related to the fraction of the droplet in contact with the surface. These are the Wenzel's angle Eq. (2.2) and the Cassie-Baxter angle Eq. (2.3).

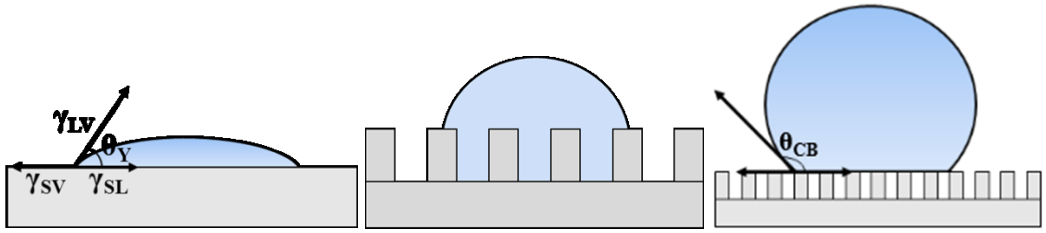

(a) (b) (c)

Figure 2.26 (a) Young's Angle θ_Y on a Flat and Homogeneous Surface, (b) Wenzel State (wetting), and (c) Cassie-Baxter State (non-wetting) with Contact Angle θ_{CB}

2.5.2 Wenzel model

Wenzel [73] modified Young's equation for a rough surface, where the real contact area between solid and liquid are larger than the apparent surface area. By assuming wetting contact, top liquid can always invade into the gap on rough surface completely as shown in Figure 2.26 (b).

$$\cos\theta_w = r\cos\theta \tag{2.2}$$

2.5.3 Cassie-Baxter model

The Cassie-Baxter angle [74] can be determined through experimentation. It is the contact angle made by a droplet on a rough surface, whereby there exist air pockets trapped between the surface of the droplet and the surface itself (i.e. the drop does not wet the surface completely), shown in Figure 2.26 (c).

$$cos\theta_{CB} = f_1 cos\theta_1 + f_2 cos\theta_2 \tag{2.3}$$

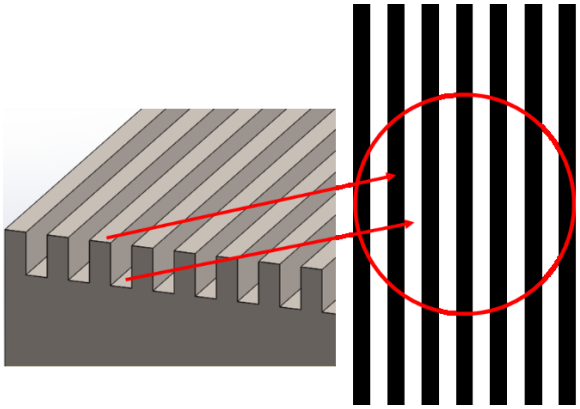

Figure 2.27 Illustration of Contact Area Fraction f: (a) Channel Design, (b) Top View of the Channel Design

When a water droplet is dropped on a target surface, it will touch both solid part (as shown in black color) and air part (as shown in white color). f is the fraction of solid surface area wet by the liquid. The red circle indicates the three-phase contact line.

Hysteresis is the difference between the advancing angle and the receding angle (refer to Figure 2.21). It is a characteristic of a surface chemistry and topography [75]. Not like ideal surface with just global minimum given by Young's equation (2.1), for heterogeneous surfaces, the inhomogeneities lead to multiple local free energy minima and cause pinning of three-phase contact line. Contact angle hysteresis depends on both thermodynamic variables and the achieved state [76]. For heterogeneous surfaces, local energy barriers have to be overcome before wetting more surface area. Models for ideal grooves surfaces [77] and statistical approach were developed for surfaces with randomly distributed defects [78]. Besides roughness and heterogeneities, some other factors were also discussed in recent years including adhesion [79], liquid adsorption [80], molecular rearrangement [81] and droplet evaporation [82]. Surfaces with lower solid area fraction can lead to lower hysteresis [83]. But this relationship is probably only effective when the structure scale is in lower than 10μm [84] or in nanoscale [85]. It means that hysteresis will be decreased as the solid area fraction

decreases. But the solid area fraction decrease should be from low microscale or nanoscale structures.

2.6 Summary

In this chapter, three main applications of hydrophobic surfaces are introduced (ice-covering-proof, self-cleaning and drag reduction). The common hydrophobic surface fabrication methods are reviewed. Measurement methods for static and dynamic contact angle are then introduced. The sessile drop method will be used in Chapter 3 and Chapter 4. The contact-angle measuring system used in the system is based on sessile drop method. Several factors that may affect static contact angle and hysteresis were discussed. Some theories about static contact angle and hysteresis are presented. This chapter lays a foundation for the following chapters.

Chapter 3

Hydrophobic Surfaces from Laser Fabrication

3.0 Introduction

This chapter will demonstrate that laser-machined stainless steel surfaces exhibit excellent hydrophobicity even with relatively simple microstructural designs. Laser fabrication developments in hydrophobic surfaces were introduced in 3.1. Four micro structure designs including channel, pillar, varied channel and varied pillar are presented in 3.2. Microscale structures with varied height features were designed instead of the classic channel and pillar designs. 17-4 PH stainless steel was laser machined to produce channels or pillars (100 μm pitch), with either uniform heights (100 μm) or alternating heights (between 100 μm and 50 μm). During machining, the high-power laser beams also created sub-micron features on the microstructures, leading to hierarchical, multiscale surface structures. These surfaces showed good hydrophobicity; measured static contact angles of water on these surfaces are over 130° without any coating, compared to near 70° on the stainless steel surface without the multi-scale surface structures. Patterned surfaces show lower hysteresis than smooth but this change is not obvious in the four laser-machined surfaces. Coating application process is presented in 3.3. After coating, the contact angles of all surfaces increased and hysteresis dramatically decreased. Contact angle measurement and analysis are discussed in 3.4. Since liquid-repellent surfaces have many engineering applications but are often difficult to produce on common metals such as steel, these results have more potential industrial benefits.

3.1 Laser Fabrication Developments in Hydrophobic Surfaces

Hydrophobic surfaces have many potential engineering applications including drag reduction for aircraft [86], submarines [87], and subsea pipes [88]. Hydrophobic surfaces can be found in nature. For example, lotus leaf surfaces are superhydrophobic with a combination of micro-scale and submicron-scale textures and hydrophobic surface chemistry. In recent years, development of hydrophobic surfaces has attracted the interest of many researchers [89]. Overall two different approaches have been investigated for hydrophobic surface design: either applying coatings with low surface energy, or developing multi-scale, sub-micron topography on a surface. For the latter method, a desirable multi-scale structure traps pockets of air to reduce the solid–liquid contact area, thereby leading to a hydrophobic surface. Classic analytical models have been developed for these phenomena, such as the wetting model by Wenzel [90] for moderate roughness and the Cassie and Baxter model [91] for high roughness. There are many ways to fabricate multi-scale structures on different material surfaces by using mechanical, chemical or electrochemical approaches. In this study, we developed hydrophobic surfaces for an important engineering metal (stainless steel) using laser machining to produce multi-scale structures.

In laser machining, material from metallic samples is removed with laser irradiation. It can be used for almost all metals and can make complex shapes [92] with high-accuracy. Many laser machining systems are capable of fabricating microscale structures (<100μm), making them suitable for producing hydrophobic surface structures. Different structures can be produced by adjusting laser exposure parameters [93]. Vorobyev and Guo [94] created multifunctional surfaces on several metals (brass, platinum, titanium) with femtosecond laser pulses. The hierarchical nano- and micro-structures lead to both super-hydrophobicity and high light absorption. In developing a hydrophobic silicon surface with a laser, Wang et al. [95] found

that increasing laser pulse frequency resulted in measured static contact angles different from the original 64° (smooth surface) to 98° and then back to 76° on the machined surfaces. Similar wetting transitions were found by Bizi-Bandoki et al. [96] when applying femtosecond laser irradiation on AISI 316L stainless steel. Besides laser pulse frequency, scan speed can also affect material surface wettability by controlling spot overlap. Circular grooves can transform into radial grooves under higher scan speed, thus providing better wettability [97].

By applying different laser frequencies, many structures, such as pillars, channels, and ripples, with different periodicity and size, can be created [98]. The most important parameters for hydrophobic structures are the height of the structures and the distance between them [99]. Bhushan and Jung showed that air pocket formation probability tends to vary inversely with spacing between bumps [100]. By analyzing surface roughness, adhesion and friction data for both hydrophobic and hydrophilic surfaces, they concluded that the combination of low surface energy material and proper roughness is the key for high hydrophobicity.

Many current studies on hydrophobic surface development are limited to coatings or structured surfaces on silicon or other special materials (such as platinum and titanium). There are only a few studies on common industrial metals such as steels. Our current study aims to achieve good hydrophobicity on steel (17-4 PH stainless steel) with relatively simple microstructures fabricated with laser machining. In addition to the common pillar and channel designs, two new structures with alternating heights of pillars and channels are also designed, fabricated and tested. The static contact angles of these surfaces are analyzed and compared.

3.2 Surface Structure Design and Laser Fabrication

Microscale channels and pillars, as shown in Figure 3.1 (a) and (b) respectively, are two common structures for hydrophobic surface design and are also used in this study. As indicated in the drawing, the channels have a depth of 100 μm and a width of 50 μm, with 100 μm pitch. The pillars have square cross-sectional area of 50 μm × 50 μm and have a height of 100 μm, with 100 μm pitch. This study modified the microchannel and micro-pillar designs and developed the varied channel and varied pillar structures. With these new designs, the structures have alternating channel depths or pillar heights, from 100 μm to 50 μm, leading to overall approximate V shapes. Limited by equipment resolution capabilities, we used a width of 50 μm, with 100 μm pitch in our design. We hypothesized that these new structures could help to trap more air and achieve good hydrophobicity and drag reduction if used in flow systems.

The fabrication process of these micro-structured surfaces consists of three main steps: bulk cutting, grinding and laser machining. Each of these three steps was carried out by the Shenzhen KEYAN company, according to our specifications. In the first step, a wire-electrode cutting technique was applied in cutting a large piece of stainless steel (17- 4 PH) into thirty smaller pieces (each 20 mm × 10 mm × 5 mm, the dimensions of our experimental samples). In the second step, each small sample was ground with a grinding machine to make all 6 surfaces smooth (~7.9 μm RMS roughness based on profilometer data). Smooth finish and degree of parallelism of the prepared surfaces are important since our targeted hydrophobic structure is on the micrometer scale, and a coarse surface would affect the final machined structure. After grinding, a sample's degree of parallelism can reach 0.015 mm/1000 mm between the finished surface and the base surface. In the third step, a BMF20A/B Fiber Laser machine was used to machine the designed microscale structures on the prepared small samples. Only one side, with surface area of 10 mm × 20 mm, was machined on each sample. To start laser machining, a sample was placed under the

laser device, and then it was brought into focus of the laser lights for machining. In this study, the following parameters for the laser were used: laser power = 12 W, wavelength = 1060 nm, frequency = 20 kHz, marking speed = 600 mm/s. With this machining procedure, samples with the four different micro-structures shown in Figure 3.1 were fabricated for wettability testing.

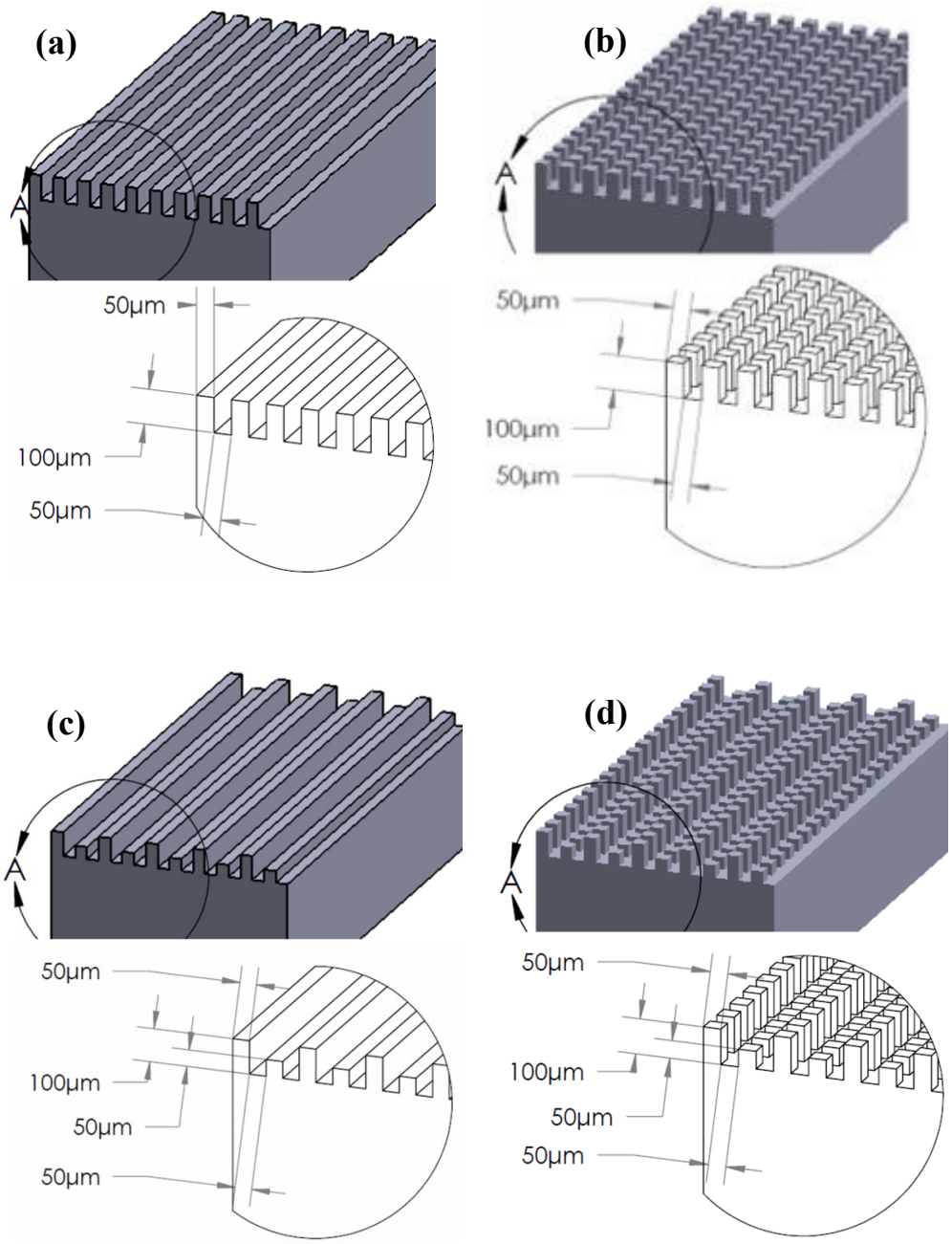

Figure 3.1 Four Microstructure Designs: (a) Channel, (b) Pillar, (c) Varied Channel, and (d) Varied Pillar

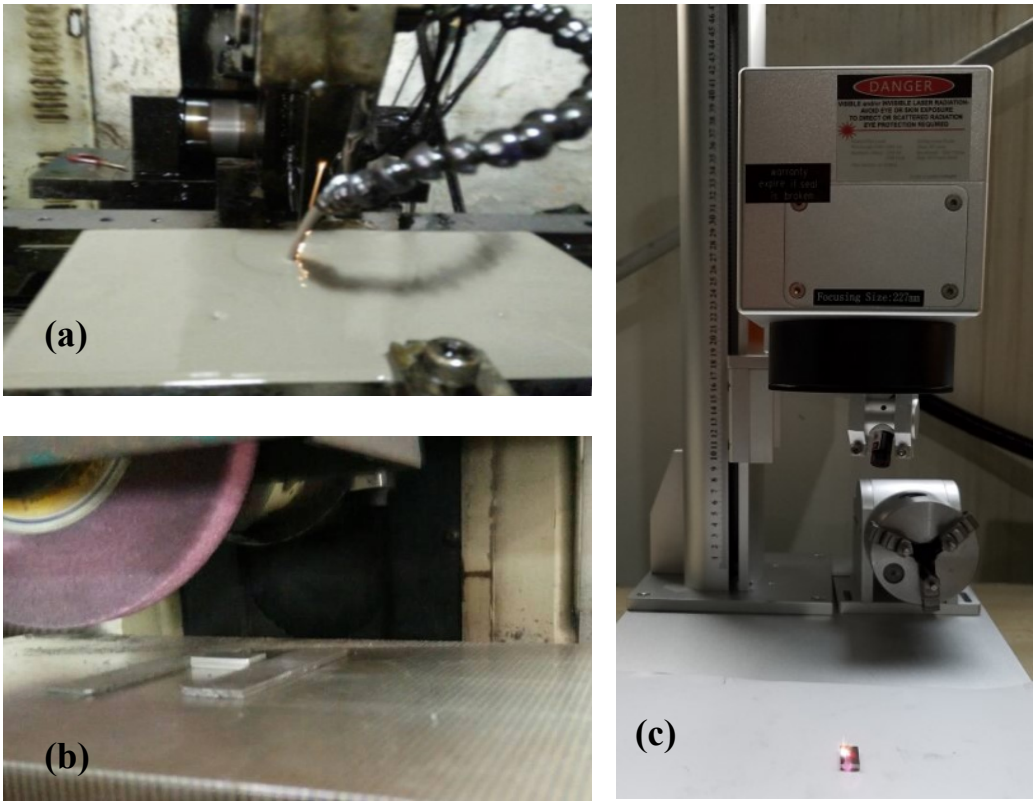

Figure 3.2 Laser Machining Steps: (a) Bulk Material Cutting and Trimming, (b) Grinding to Get Smooth Working Surfaces, and (c) Laser Machining to Produce Microstructures

3.3 Coating Application in Laser Method

Coating method can further increase surface hydrophobic ability. Applying coating with low surface energy can significantly change contact angle and hysteresis. In this research, the coating method was also implemented to further increase contact angles and decrease hysteresis. The coating we studied was a Metal Repellency Treatment coating from Aculon, a company commercializes unique surface and interfacial materials. Aculon Coating was tested on stainless steel smooth surface to verify its repellent ability. The contact angle of smooth surface was increased from 73±3° to 121±3°. Due to its excellent performance in static contact angle, dynamic contact angle tests were also conducted on laser-machined surface. The coating was applied to the laser machined surfaces by fully immersing the samples in the coating

solution for 30 seconds then withdrawn at a steady rate to ensure even coverage, followed by air dry. The coating cannot be over applied because it is a self-limiting reaction and does not crosslink to form thicker layers. The chemical composition of this coating provided by the Aculon company is 50-52% Ethanol, mixture of 42-46% 2-(difluoromethoxymethyl)-1,1,1,2,3,3,3-heptafluoropropane and 4-methoxy-1,1,1,2,2,3,3,4,4-nona-fluorobutan), 2-3% 2 propanol and 2-3% Methanol.

3.4 Contact Angle Measurement and Analysis

The contact angle of a droplet on a surface indicates the wettability of the surface. The contact angle measurements were done with the OCA 15EC contact angle instrument from Dataphysics (Germany). To measure the static and dynamic contact angles of water on a sample surface, the sample should be laid flat on a smooth and clean surface, in line with a camera at approximately 10 cm. For typical channel and varied channel, the camera is parallel to the grooves. The camera focus and light source should be adjusted for optimal clarity and brightness of images. A water droplet is dosed using the “dispense” function in the software, with a dispense rate of 2µl/s. All measurements were conducted under a room temperature of 20 °C. The water drop was left to sit 2-5 seconds before the image was taken. The droplet would then be whisked away using a dry paper towel, the surface was given time to fully dry, and then the next test performed. The contact angle measuring system is shown in Figure 3.3.

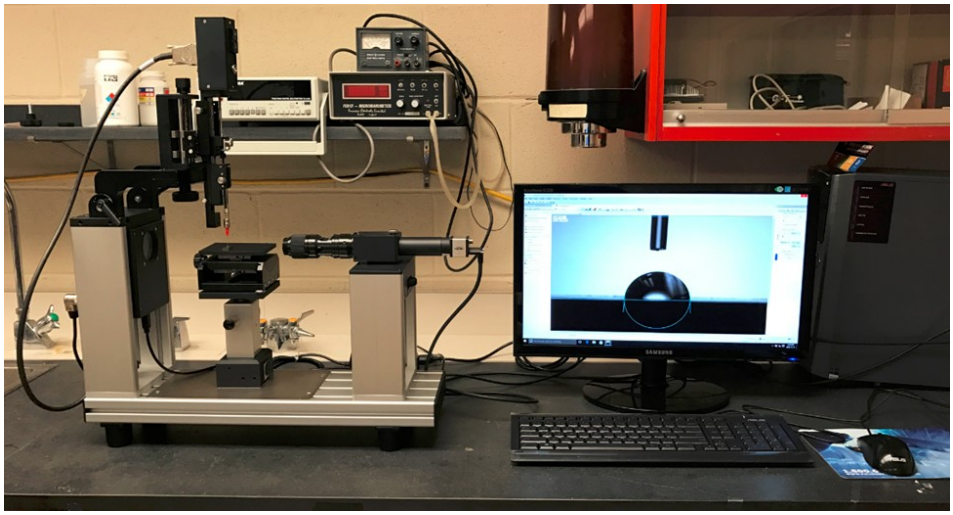

Figure 3.3 The Dataphysics OCA 15EC Contact Angle Measurement System

All four machined samples in Figure 3.1 and a baseline sample with smooth surface were tested. The reported contact angle and hysteresis value for each surface was averaged over a number of six measurements at different locations of the same sample to minimize errors caused by chemical and topographical inhomogeneities.

The goal of this work was to obtain contact angles on stainless steel that approach superhydrophobicity of $\theta_{CB} > 150°$ and this was attempted by laser machining samples of 17-4 PH stainless steel with various surface patterns shown in Figure 3.1. This created roughened surfaces that we expected could trap more air between the droplet and surface, lowering the fractional contact area. Figure 3.5 shows SEM images of the four machined surfaces with a typical measured contact angle for water on each surface. The images are obtained from a MLA 650 FEG ESEM machine with the following basic parameters in the imaging setup: BSED detector, HV = 25.00 kV, magnification = 600×, scale = 100μm. Due to the nature of the laser machining process, the actual dimensions of the machined microstructures are slightly different than the designs shown in Figure 3.1. Cone shapes resulted from the pillar and varied pillar, as shown in Figure 3.4 and Figure 3.5. The lack of exact perpendicular cuts is a result of the laser

ablation. Some irregular features and submicron structures appeared on the humps, as shown in Figure 3.6.

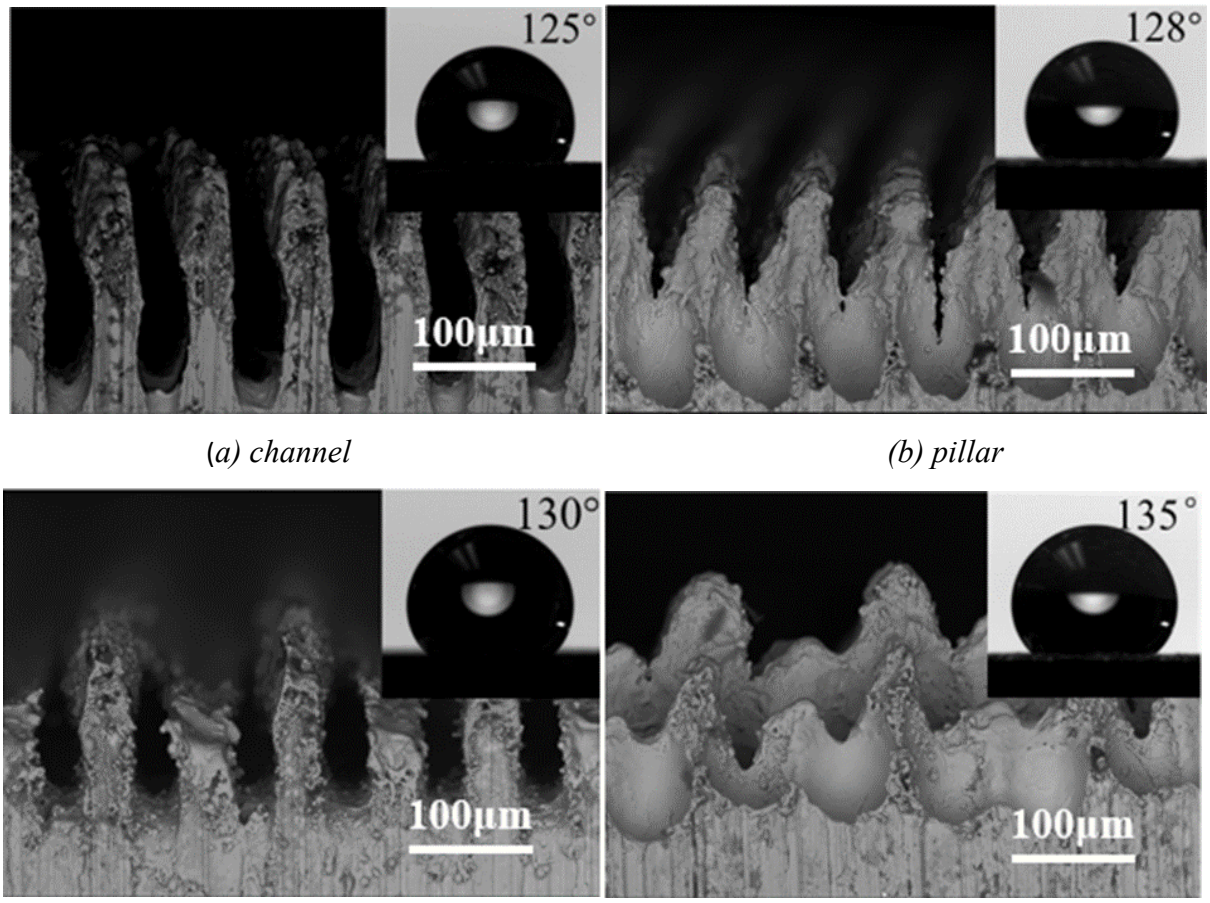

(*a) channel* *(b) pillar*

(c) varied channel *(d) varied pillar*

Figure 3.4 SEM Images of and Droplet Images on the Four Different Surface Designs: (a) Channel, (b) Pillar, (c) Varied Channel, (d) Varied Pillar

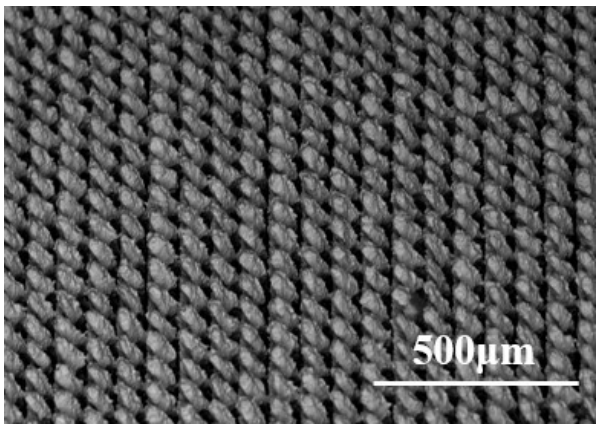

Figure 3.5 A Top-view SEM Image of the Pillar Pattern Using Back-Scattered Electron Detection

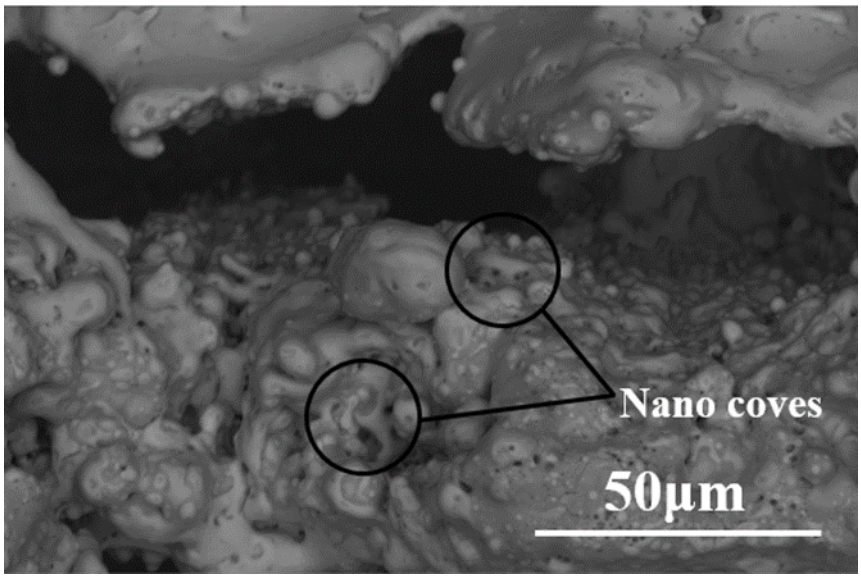

Figure 3.6 Irregular Smaller Structures Appear on the Laser-machined Pillars and Channels

More description and discussion about f can be seen in Figure 2.27. If the contact area fraction f is known for a surface, then the contact angle on it can be roughly estimated using Eq. (2.3). In this work, we call this value the "calculated" contact angle. For a droplet on an ideally smooth surface, there is no air pocket between the surface and the liquid and the contact area fraction is therefore assumed to be $f_s = 1$. For the channel design, shown in Figure 3.1 (a), the equally distributed extrudes and gaps lead to an assumption that the contact area fraction for a droplet on these surfaces will be $f_c = 0.5$. For the pillar designs, similar reason leads to $f_p = 0.25$. For these cases, we assumed that the droplet does not extend down into the grooves far enough to touch the bottom surface. For the varied channel and varied pillar designs, two wetting situations can be considered, leading to two different assumptions for the contact area fraction. Figure 3.7 (a) shows the first situation for the varied channel design. The water droplet only covers the top surface of the high humps, without touching the lower hump. With this assumption, and refer to the dimensions in Figure 3.1 the contact area fraction will be $f_{vc1} = 0.25$. In the second situation, as shown in Figure 3.7 (b), the droplet wets the top surface of the higher humps and the top surface of the lower humps. With this assumption, the contact

area fraction will be $f_{vc2} = 0.5$. Similar assumptions can be made to the varied pillar design and get $f_{vp1} = 0.125$ and $f_{vp2} = 0.25$.

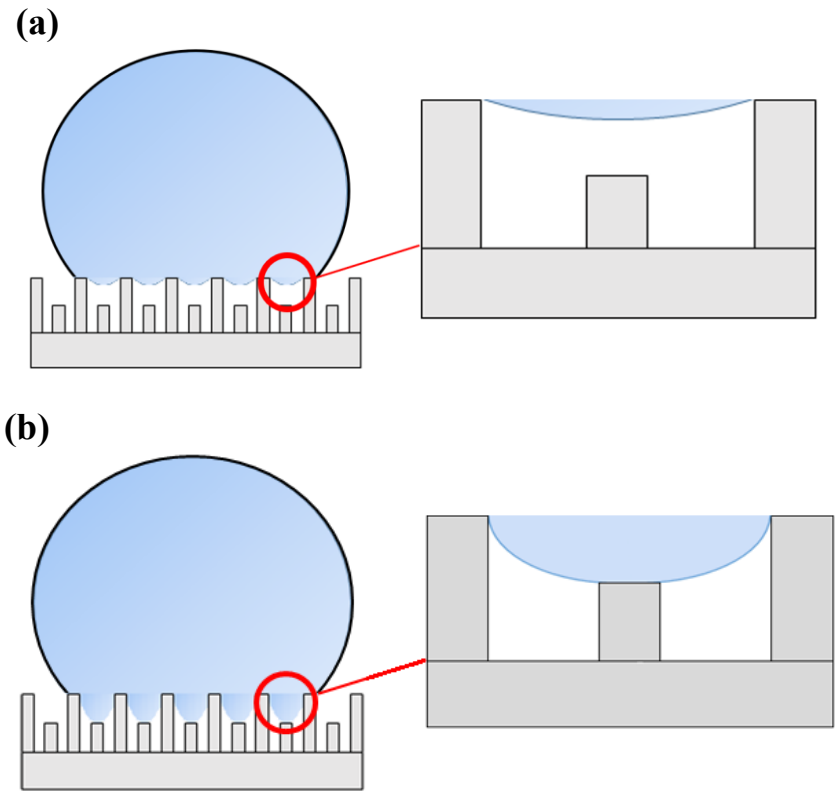

Figure 3.7 Two Wetting Assumptions for the Varied Channel Design, (a) Assumption 1 – half touch: Droplet Only Covers the Higher Hump but Does Not Touch the Lower Hump, leading to $f_{vc1} = 0.25$, and (b) Assumption 2 – full touch: Droplet Covers the Higher Hump and the Lower Hump, Leading to $f_{vc2} = 0.5$

There were two main sources of uncertainty in the contact angle measurement: (1) image resolution error, δ_{CA_Re}, due to the uncertainties in defining the droplet and surface edges, limited by the resolution and contrast of the droplet image, and (2) the precision index error, δ_{CA_Sd} (or standard deviation), based on multiple measurements of different droplets on the same surface. The total uncertainty of our contact angle measurements, δ_{CA_Total}, was obtained by combining these uncertainty terms using Eq. (3.1).

$$\delta_{CA\_Total} = \sqrt{(\delta_{\mathrm{CA\_Re}})^2 + (\delta_{\mathrm{CA\_Sd}})^2} \tag{3.1}$$

OCA 15EC uses a manually adjusted scroll bar to line up the contact angle measuring template with the droplet image, and thus a $\delta_{\mathrm{CA\_Re}} = \pm 1°$ was a typical uncertainty for any given droplet measurement. It is important to note that for any sample surface, the range of contact angle values for different droplets had a spread of near 10°, which is significantly more than the image resolution error of ±1° for any individual droplet measurement. Calculating the standard deviation $\delta_{\mathrm{CA\_Sd}}$ was done by taking N (N = 6 in this study) repeated measurements of contact angle. The standard deviation is then

$$\delta_{\mathrm{CA\_Sd}} = \sqrt{\left(\frac{\sum_{k=1}^{N} \left(x_k - \bar{x} \right)^2}{N-1} \right)} \tag{3.2}$$

where $\bar{x}$ is the average value of the 6 contact angle measurements taken on a single sample, and x_k (with k ranging from 1 to 6) is the contact angle of a single test on a unique droplet.

Table 3.1: Contact Angle Data Before and After Coating for the Four Microstructured Surfaces. Measured Contact Angles are Compared with Estimated Ones using Eq. (2.3) and Assumed Contact Area Fractions.

		Smooth	Channel	Pillar	Varied Channel	Varied Pillar
Uncoated	Measured	73±3°	125±5°	128±5°	130±5°	135±6°
	Half touch		111°	133°	133°	147°
	Full touch	73°			111°	133°
Coated	Measured	121±3°	138±5°	142±4°	145±4°	152±4°
	Half touch		139°	152°	152°	160°
	Full touch	121°			139°	152°

Table 3.1 shows the measured contact angles of water on each of the four laser machined surfaces with microstructures before coating, as well as a comparison with the calculated (Cassie-Baxter) contact angles using the contact area fractions discussed above. The results indicate that good hydrophobicity can be achieved on stainless steel surfaces with relatively

simple laser machined microstructures. Contact angles on the smooth surface without microstructures were 73° ± 3°. After laser machining, all four surfaces with microstructures showed hydrophobic interactions with water, with static contact angles near 130°.

Comparisons between the measured contact angles and estimated values from the Cassie-Baxter model in Eq. (2.3) helps to define some aspects of the wetting characteristics of the microstructured surfaces. For example, with the varied channel design, the measured contact angle of 130°±5° and the calculated value of 130° (with partial contact (Assumption 1 discussed earlier) agrees well. This may indicate that with this microstructure the water is only in contact with the higher humps, as shown in Figure 3.7 (a). However, for the varied pillar design, Assumption 2 (full touch) leads to an estimation that is closer to the measured contact angles. This indicates that water droplets on these surfaces may cover the higher pillars and the lower pillars. For the channel design, the measured value is significantly higher than the value predicted by the Cassie-Baxter model. The wetting characteristics would likely be different along the top of a single channel compared with the side of the droplet that spans many different channels. Furthermore, the SEM images in Figures 3.4, 3.5, 3.6 show that there are many different length scales for the roughness that we do not take into account with our simple model.

After coating, all microstructured surfaces show higher contact angles than before. With varied pillar structure and coating, the sample shows superhydrophobic ability which is 152°±4°. Varied channel and varied pillar shows similar wettability with the common channel and pillar design. In this case, the Cassie model can predict channel design very well. For pillar design, calculated value is a little higher than the measured value. The calculated values from Assumption 1 and Assumption 2 are similar for varied channel. For varied pillar, Assumption 2 is still better than Assumption 1 in data prediction.

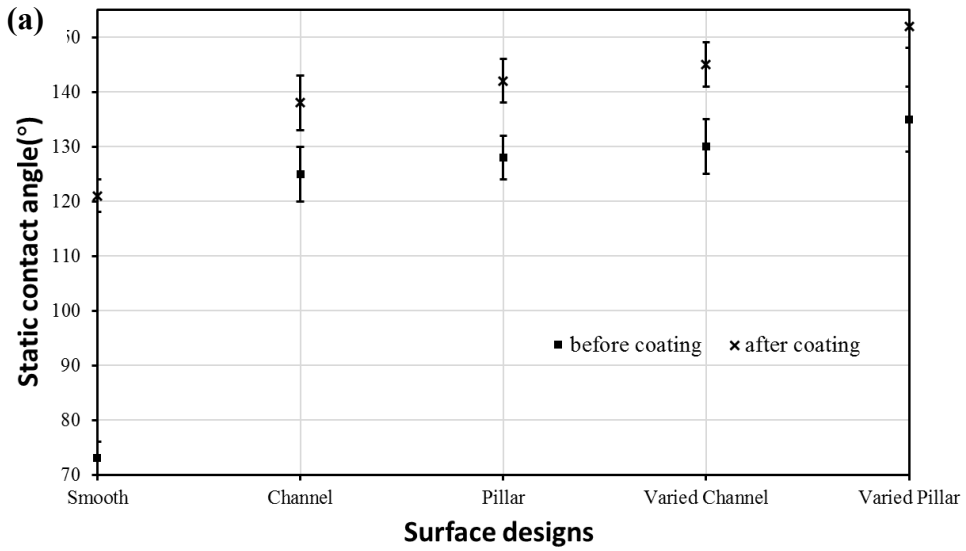

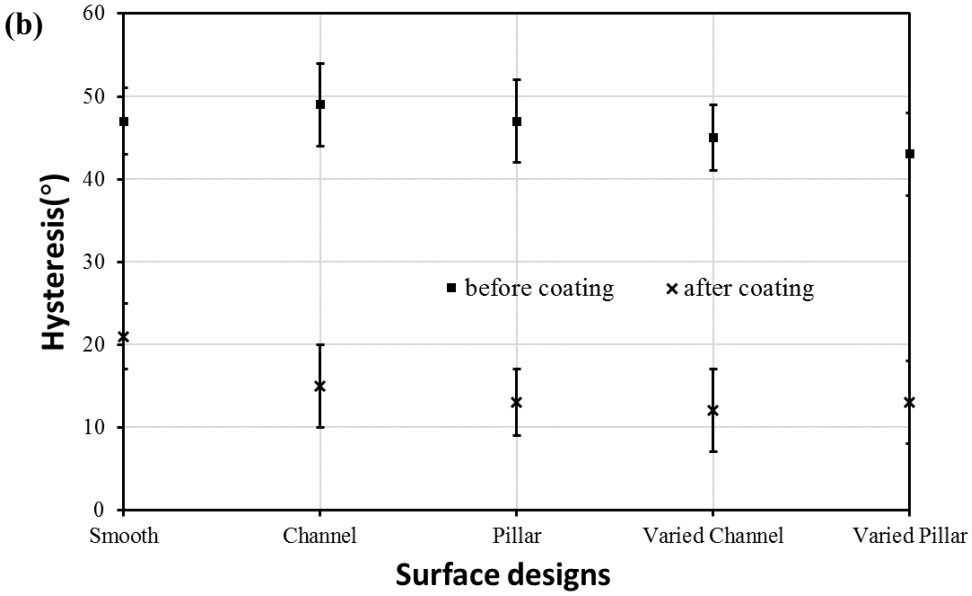

Figure 3.8 Effects of Aculon Coating on the (a) Contact Angles and (b) Contact Angle Hysteresis of the Laser Machined Surfaces with Different Microscale Roughness Structures

From Figure 3.8 (a), the coating method can increase the contact angle significantly on the all five samples, especially for the smooth one. For the four designs fabricated by laser machining, there are still increase but it was not obviously. Considering that the increase following coating on the four laser treated surfaces are almost equal, the coating method seems to have the same positive effect on the four structures. After coating the four laser treated samples, SEM were

conducted again to detect the surface structure change in microscale and nanoscale from the coating process, but no obvious structure change was found on the four samples. The coating is indeed optically clear. Thus, all the water contact angle increases on the four laser treated surfaces mainly rely on chemical change, not the microscale structure change. Based on the change on the smooth surface, the coating effect is more effective under a contact angle of 120°. For varied channel, half touch assumption is more suitable. However, for varied pillar design, full touch assumption is better. One possible reason is the deformation of varied pillar is heavier than that of varied channel. Top liquid is easier to drop down to the lower pier. The hysteresis changes are shown in From Figure 3.8(b). The hysteresis results are close to the control and the difference is not obvious within the four different patterned surfaces. In this research, all four laser-machined surfaces own sub-micron structures created by laser as shown in Figure 3.6. The coating method can dramatically decrease the hysteresis and the hysteresis value for all laser machined samples are lower than the smooth sample.

3.5 Summary

In this chapter, both laser method and coating method were applied to increase contact angle and decrease hysteresis on stainless steel. Channel, pillar and designs with varied height features were laser machined and coated, and the smooth surface is used as control. The experimental results showed that all the four microscale structures produce hydrophobic responses for mm-sized water droplets on 17- 4 PH stainless steel. The values of these contact angles, all near 130°, are consistent with a simple Cassie-Baxter model for wetting that assumes only fractional surface area contact between the droplet and the surface. Thus, even though SEM images showed considerable differences in the sub-micron surface morphology of the machined surfaces, those smaller surface features do not appear to influence the contact angle of mm-sized water droplets on these surfaces. Varied channel and varied pillar show similar

wettability as common channel and pillar design. After coating, the contact angles of all samples were increased, especially for the smooth one which significantly increased from 73±3° to 121±3°. For laser machined samples, the coating effect is not so obvious, e.g. the contact angle of coated channel sample only increases from 125±5° to 138±5°. The coating effect seems to be more effective under a contact angle of 120°. The hysteresis values of the four patterned surfaces are close. Further research may focus on the nanostructure effect on laser-machined surfaces. The coating method can dramatically decrease contact angle hysteresis by nearly 30°.

Chapter 4

Hydrophobic Surfaces from Sandblasting Fabrication

4.0 Introduction

In this chapter, the sandblasting method is used to create different textures. The materials used in this research for sandblasting are 17-4 PH stainless steel and A350 Gr Lf 2 carbon steel. Sandblasting fabrication applications, process and parameters are discussed in 4.1. Standoff distance between the sandblasting spray gun and the sample is considered (10 mm, 20 mm, 30 mm). In 4.2, developments of sandblasting methods for hydrophobic surface fabrication are presented. Coating method is also applied in sandblasting samples. The coating application process is shown in 4.3. The Aculon coating was applied to reduce the samples' surface energy and further increase the contact angles and decrease the hysteresis. Contact angle measurement and analysis is discussed in 4.4. All stainless steel samples showed higher hysteresis after sandblasting. Micron-scale and sub-micron structures play an important role in static and dynamic contact angles. This coating method is effective for both materials with achieving higher static contact angle and lower hysteresis. This chapter demonstrates that sandblasted stainless steel surfaces exhibit excellent hydrophobicity but the sandblasting method is not suitable for carbon steel.

4.1 Sandblasting Fabrication Applications, Principle, Process and Parameters

Sandblasting is a processing method that uses a compressed air jet containing micro-abrasives [101]. Blasting materials are usually called abrasive media; when sprayed by a nozzle, material will be partially removed from the smooth surface under high injecting pressure. The sandblasting process can protect workpieces to the greatest extent possible from heat effects and can minimize the deteriorated layer formed due to the fabricating process. Its basic principle is to utilize the random motion of sand to impact and roughen the target surface. Due to the erratic movement and irregular shape of the abrasive particles, the result will also be an uneven surface morphology.

Many sandblast machining systems are capable of fabricating microscale structures (<10μm), making them suitable for producing hydrophobic surface structures. Different roughness values can be produced by adjusting the sandblasting machining parameters (such as the injection pressure, particle size, impacting angle, standoff distance, operation time, etc.) while accounting for different material characteristics (hardness, Poisson's ratio, etc.). The surface roughness led to a better bond strength of coating. Carbon steel material was also used as a substrate material by Shkodkin et al. [102], who found a correlation between coating and roughness. For example, beyond bonding characteristics, they also discussed that substrate surface roughness may stimulate metal coating deposition. Instead of single injection particles, they chose a mixed ceramic/metal-powder to create a thicker coating. But Marmur [103] pointed out that only a few types of roughness topographies can help to transit from Wenzel state to Cassie state. Some key parameters that can dominate the wettability are summarized by Liu et al. [104]. In microscale structure design: shape, size, height, pattern period can affect wettability. For some advanced surface designs, hierarchical or multiscale structure can also play effects. Xiu et al. [105] found for structures created randomly, the structures often show

incline characteristic on the substrate. The inclined angle of structure wall can affect contact angle results as well. Based on these reasons, roughness is not used as a quantized measure to distinguish different treated samples.

This research mainly contains two experimental parts: sandblast fabrication and contact angle measurement. In the sandblast fabrication part, there are two groups: the stainless steel group and the carbon steel group. In each group, there are 6 samples made under every sandblasting standoff distance treatment and 6 untreated samples set as the control group. Therefore, there are 24 samples in total in each group, 12 sandblasted samples and 12 untreated ones. Three samples made under the same treatment conditions were used to prove repeatability. Each carbon steel sample measures 35 mm long×35 mm wide×6 mm thickness. Each stainless steel sample measures 30 mm long×30 mm wide×7 mm thickness. The group information is summarized in Table 4.1.

Table 4.1: Sandblasting Fabrication Group Information

	Number of samples	
Standoff Distance(mm)	Without coating	Coating
10	3	3
20	3	3
30	3	3
Without sandblasting	3	3

Sandblast fabrication was done with the micro-Abrasive sand blaster from the Vaniman company. The whole fabrication process was conducted in a sealed box as shown in Figure 4.1.

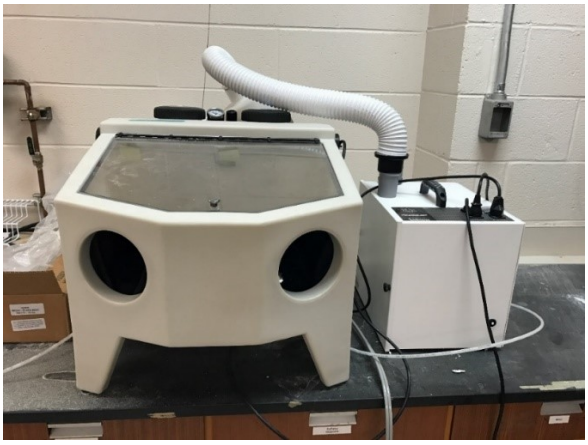

Figure 4.1 The Micro-Abrasive Sand Blaster

To fabricate textures on a sample surface, the sample was laid flat on a smooth and clean surface perpendicular to a hand-held spray gun. In this research, a holder was used as shown in Figure 4.2 to fix the hand-held spray gun and make sure it was vertical to our target surface. The holder can adjust standoff distance. The spray pressure was set as 100 psi. Aluminum Oxide Abrasive Blasting Media was chosen as the abrasive particle of 45-140 mesh size.

Figure 4.2 The Spray Gun Holder

Each sample was sandblasted using four steps as shown in Figure 4.3 to make the surface finish even and uniform. Since the spray range is limited, the sample should be sprayed line by line in each step.

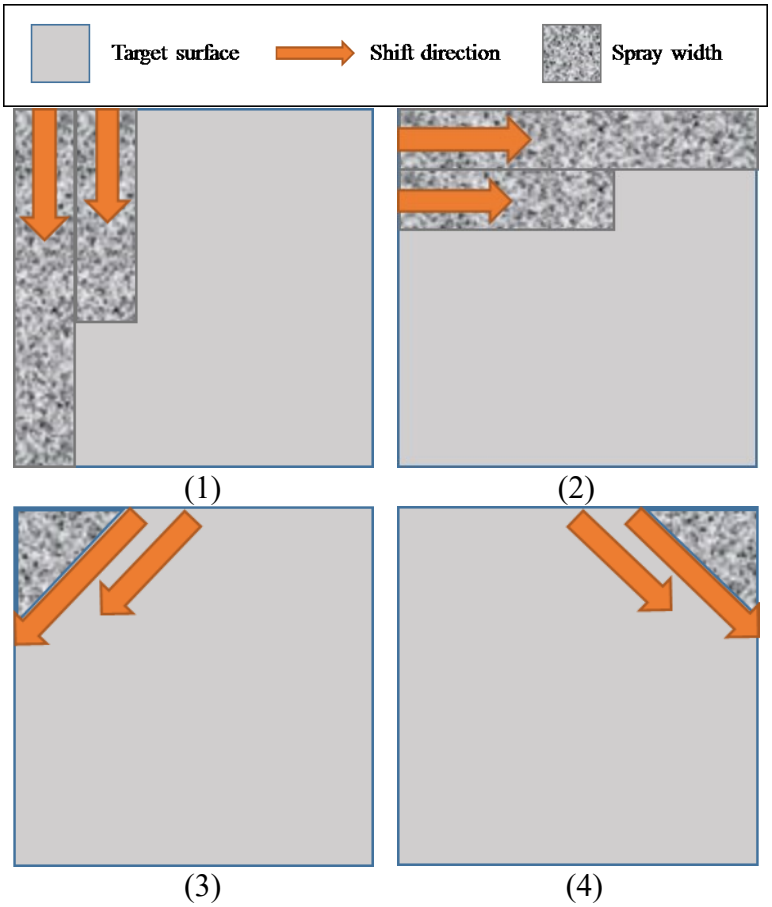

Figure 4.3 (1) Horizontal Moving Direction, (2) Vertical Moving Direction, (3) Diagonal Moving Direction, and (4) Diagonal Moving Direction to the Opposite

After sandblasting, a scanning electron microscope (SEM) was used to determine the textures formed by the abrasive particles. In this research, two kinds of cracks were found. The Aluminum Oxide Abrasive Blasting Media used in this research has irregular shapes in a microscopic view. Some parts of abrasive media are sharp but some are rounded. If the sharp abrasive particles with high kinetic energy hit the target surface, a crack with an acute angle may be formed as shown in Figure 4.4 (a) when the impact is beyond its compressive strength. Abrasive particles with rounded surfaces may lead to plastic deformation and create cracks as shown in Figure 4.4 (b). The two sand particles (a) and (b) impact on substrate and left the two different cracks. The sand particles will be blown away with compressed air. Figure 4.5 shows SEM images of the sandblasted surfaces. The two kinds of cracks show the surface changes from side view.

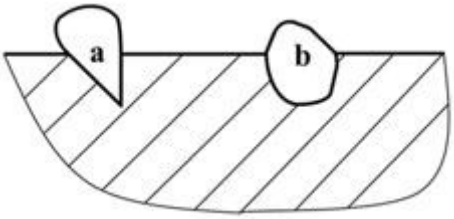

Figure 4.4 Schematic of the Two Kinds of Cracks: (a) Acute Angle, (b) Blunt Angle

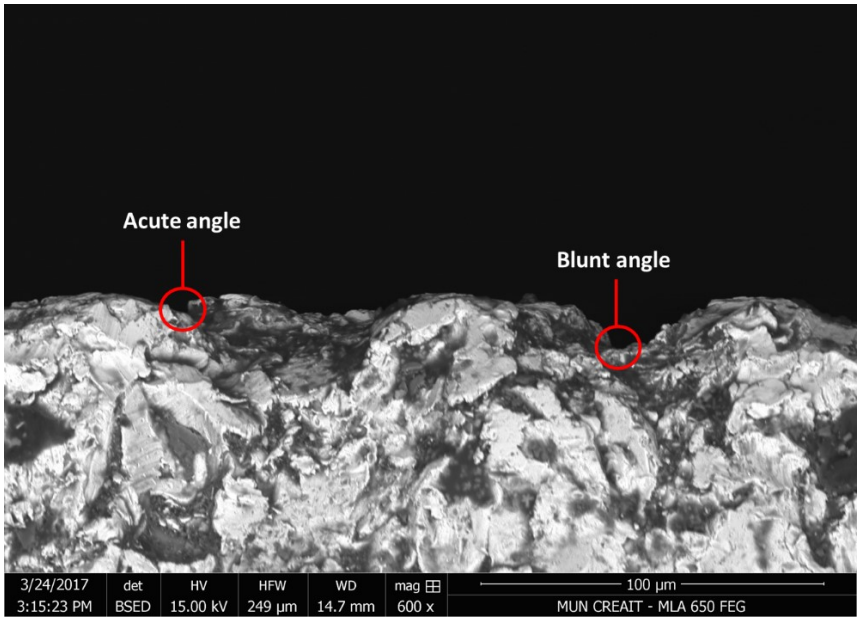

Figure 4.5 SEM Image of the Sandblasted Material Using Back-scattered Electron Detection. The Sample is Made of 17-4 PH Stainless Steel, Pressure 100 psi, Injection Angle 90°, Standoff Distance 10 mm

4.2 Sandblasting Fabrication Developments in Hydrophobic Surfaces

Sandblasting can be used for almost all metals, such as carbon steel, aluminum, titanium, cast iron and many other common materials including glass, resin, Poly (methyl methacrylate) (PMMA) [106], PolyEtherEtherKetone (PEEK) [107]. It is also widely used with zirconia ceramic, a dental material. The universal applicability of zirconia ceramic makes it become an ideal material in precision finishing and fabrication. With respect to steel, Varacalle et al. [108] experimentally investigated the effects of blast media, blast pressure, and working distance on surface roughness. Moreover, they studied the bond strength of the coatings. The results

illustrated that using the metal grits can achieve the highest bond strength for zinc-aluminum coatings. Sandblasting has also been widely used in another common material in industry: aluminum. Superhydrophobic contact angles were obtained on sandblasted porous alumina by Kim et al. [109]. In their experiment, the contact angle was approximately 165° and the sliding angle was less than 2°.

In recent years, some developed and advancing materials such as titanium have been a subject of much interest for many researchers. Barranco et al. [110] smoothed the sharp edges of blasted Ti6Al4V alloy surfaces. The effect of the impact energy of the blasted particles was determined and proved to increase the roughness and modify the chemical composition of substrate. Sandblasting also has applications in the dental material zirconia ceramic [111-112]. Aktas et al. [113] investigated the adhesion of zirconia core ceramics. The results showed metal–ceramic adhesion was better than zirconia–veneer ceramic combinations, in both bond strength and failure types.

4.3 Coating Application in Sandblasting Method

In this research, the Aculon coating method was also implemented to further increase contact angles and decrease hysteresis on sandblasted samples. More description about Aculon coating application process can be seen in Section 3.3.

4.4 Contact Angle Measurement and Analysis

As the textures are created by abrasive particles randomly, droplets on the samples' surface may be distorted a little bit. The static contact angle and hysteresis values reported for each surface were based on 6 droplets per sample, each of which was measured from 4 different directions, to account possible heterogeneity due to the surface texturing.

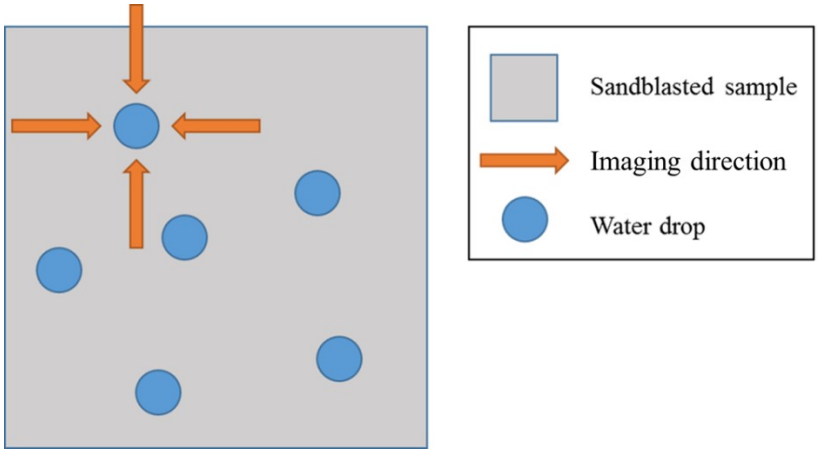

Figure 4.6 Schematic of Contact Angle Measurement for Sandblasted Samples

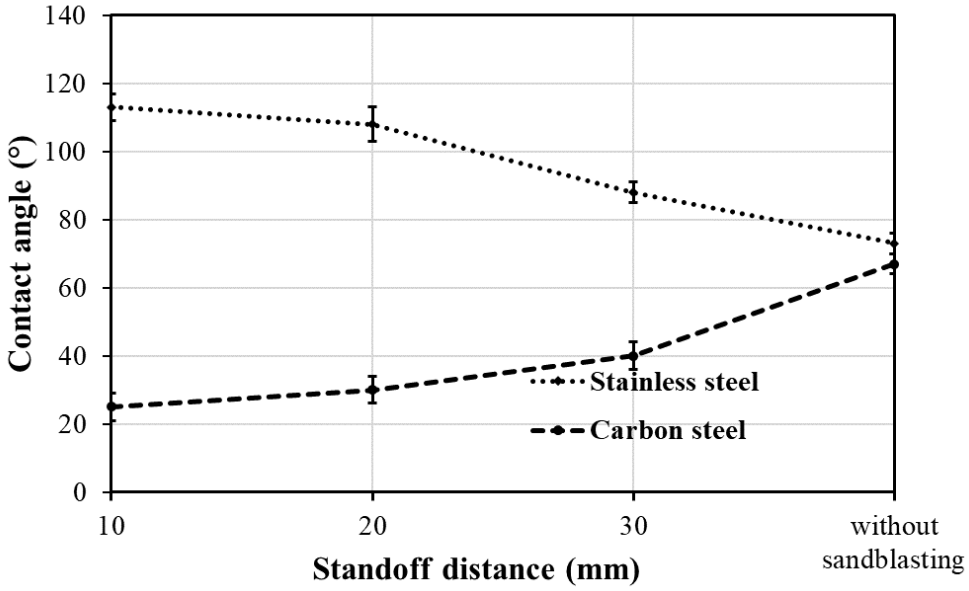

Figure 4.7 Water Contact Angle of Sandblasted Samples Before Coating

Figure 4.7 shows the measured contact angles of water on each of the sandblasted surfaces with random microstructures. Contact angles on the surface without sandblasting were 67 ± 3° for carbon steel and 73± 3° for stainless steel. After sandblasting, the contact angles for stainless steel were increased with a lower standoff distance. For carbon steel samples, the results are the opposite. Their contact angles are directly proportional to the standoff distance. The results indicate that Wenzel's model is still applicable on carbon steel samples but not for stainless steel samples. Because both materials are originally hydrophilic, based on Wenzel's model,

sandblasting should decrease their contact angles. Their different wetting performance after sandblasting may be caused by a different hardness of these two materials. Material with low hardness are easier to form coves under sandblasting process. The sandblasting process can create micro coves. As the hardness and other physical properties (impact resistance, fatigue resistance etc.) are different for these two materials, the concentration of micro coves or cracks are also different. Because hardness of the carbon steel is higher than the stainless steel, stainless steel surfaces may be more likely to form coves. The concentration of micro coves or cracks on stainless steel is probably higher than that on carbon steel. This maybe one possible reason to explain the observed phenomenon. Chromium content in 17-4 PH stainless steel is high (15% - 17.5%) and chromium content in carbon steel is negligible (< 0.3%). Chromium oxide surface is hydrophilic [114-116] and after sandblasting procedure, the content probably decreased in stainless steel which can contribute to the contact angle increase phenomenon.

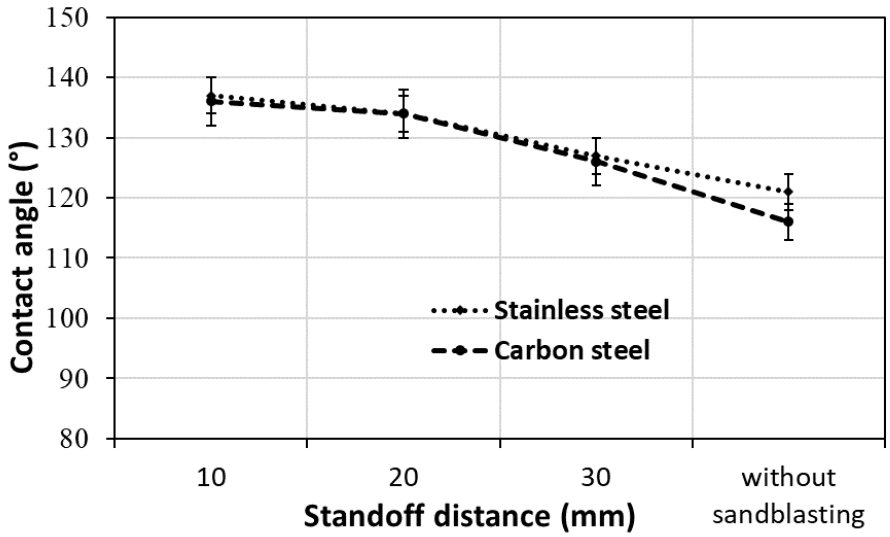

Figure 4.8 Water Contact Angle of Sandblasted Samples After Coating

In Figure 4.8, it is clearly shown that coating method is effective for both the stainless-steel samples and the carbon steel ones. The results difference of sandblasted samples made under standoff distances 10 mm and 20 mm are closer compared to those made under 20 mm and 30 mm. It is worth to notice that after the coating application, the carbon steel group also shows

the same tendency between standoff distance and contact angle. The coated samples without sandblasting for both two materials are over 90°. The original states for the two materials can be regarded as hydrophobic. After sandblasting work, the real surface area is increased. According to Eq. (2.2), parameter r will be higher after sandblasting. In this condition, the contact angle results of both materials agreed with Wenzel's model.

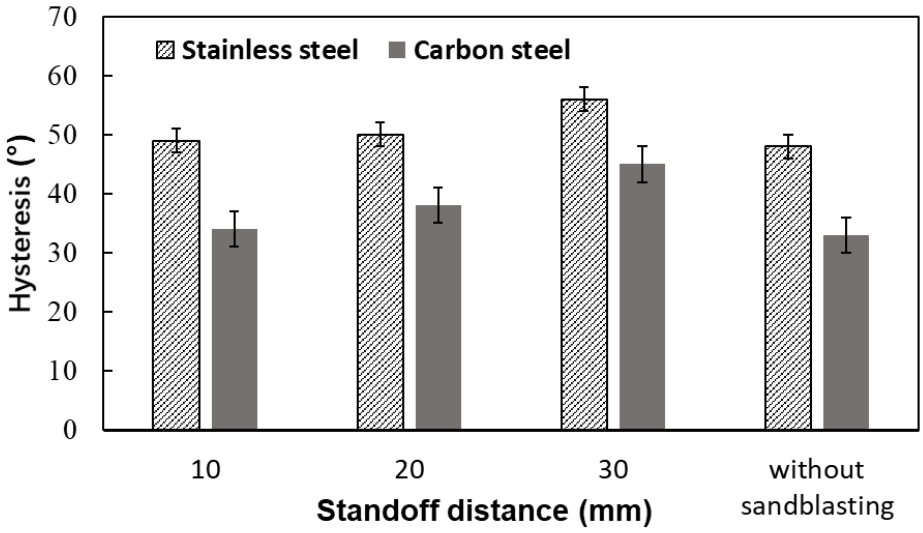

Figure 4.9 Water Hysteresis of Sandblasted Samples Before Coating

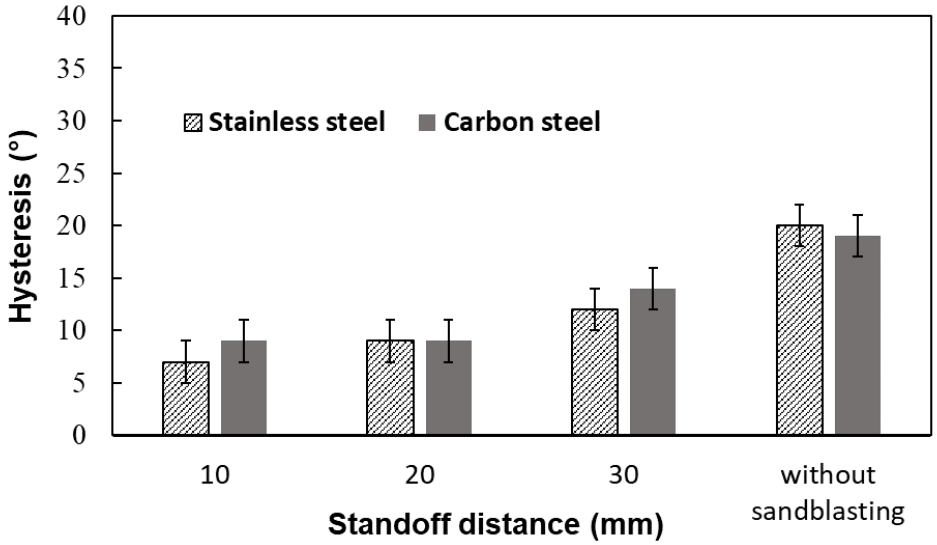

Figure 4.10 Water Hysteresis of Sandblasted Samples After Coating

From Figure 4.9 and Figure 4.10, sandblasting can increase the hysteresis by roughening the surfaces compared to the control for both materials. The coating method can dramatically

decrease the hysteresis and the hysteresis value for all sandblasted samples are quite close, less than 10°. After coating, sandblasted samples contain both air part and solid part covered by coating. However, samples without any sandblasting treatment only have solid part with coating. Adhesion between water and coated solid part is higher than that between water and air. So, the hysteresis of sandblasted samples is lower than smooth samples.

4.5 Summary

In this chapter, sandblasting was used to fabricate surface textures. For stainless steel, lower standoff distance leads to better hydrophobicity. For carbon steel samples, sandblasting increases wettability of the carbon steel, with lower contact angle from lower standoff distance. One possible reason to explain this phenomenon is the concentration of micro coves or cracks that are different for the two materials. After applying Aculon coating, the values of these contact angles are all over 120°. The hysteresis for all coated samples dramatically decreased compared with the ones without coating.

Chapter 5

Sandblasting Results Comparison with Laser Machined Samples

5.0 Introduction

In this chapter, sandblasting is compared with laser machining in hydrophobic surface fabrication. In 5.1, the process of laser machining and sandblast fabrication is compared. After laser machining and sandblasting, the SEM images of the samples (top view and side view) are compared in 5.2. Based on the comparison of contact angle and hysteresis results in 5.3, samples fabricated under 10 mm and 20 mm are better than the samples made under standoff distance of 30 mm. Sandblasting method showed similar ability to achieve hydrophobicity as laser method. Therefore, sandblasting method shows a good potential for hydrophobic surfaces mass production.

5.1 Laser Machining and Sandblast Fabrication Principle Comparison

The differences of the two methods are temperature change during operation and mass production ability. Sandblasting is a physical process via blast media impacting a surface without obvious temperature change on the target surface. But the laser method will lead to temperature increase on the surface. Temperature change may affect material properties in practical applications. During laser machining, the high-power laser beams can remove redundant material from original surface and form desired structure.

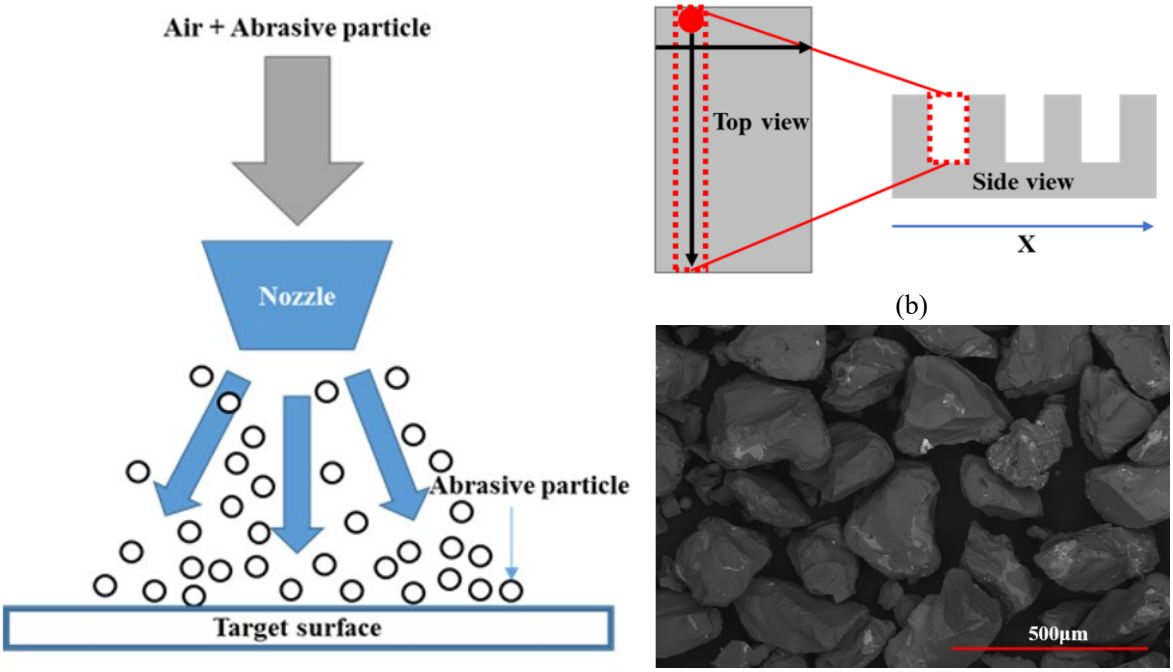

Figure 5.1 (a) Schematic of a Sandblast Process, (b) Top and Side View of Laser Machining Process, (c) Microscopic View of Blasting Media

Sandblasting is easier for mass production by adjusting nozzle size as shown in Figure 5.1 (a). To fabricate a surface with pillar structure, the material in red frame should be removed and the same process will be repeated alone x axis as shown in Figure 5.1 (b). Selecting a nozzle with higher spray range can greatly enhance output efficiency in industry. As shown in Figure 5.1 (c), the abrasive sands used in this research is irregular in microscopic view. Some parts of abrasive media are sharp but some are rounded which can lead to different structure on substrate.

5.2 SEM Results Comparison

In this research, three different standoff distances (10 mm, 20 mm, 30 mm) were applied to fabricate sandblasting samples. Lower standoff distance can provide higher impact energy on target surface. The lowest standoff distance is 10 mm which will not be harmful for the setup and the highest standoff distance is 30 mm. As shown in Figure 5.2, the treated samples from laser are not exactly as what were designed. They look like a kind of cone shape because the laser energy decreases from center point to the edge. From sandblasted SEM results in Figure 5.3, standoff distance 10 mm and 20 mm are almost same in top view and side view. The SEM images show that the edges of samples made under 10 mm and 20 mm standoff distance are more fluctuant than those under 30 mm as shown in Figure 5.3.

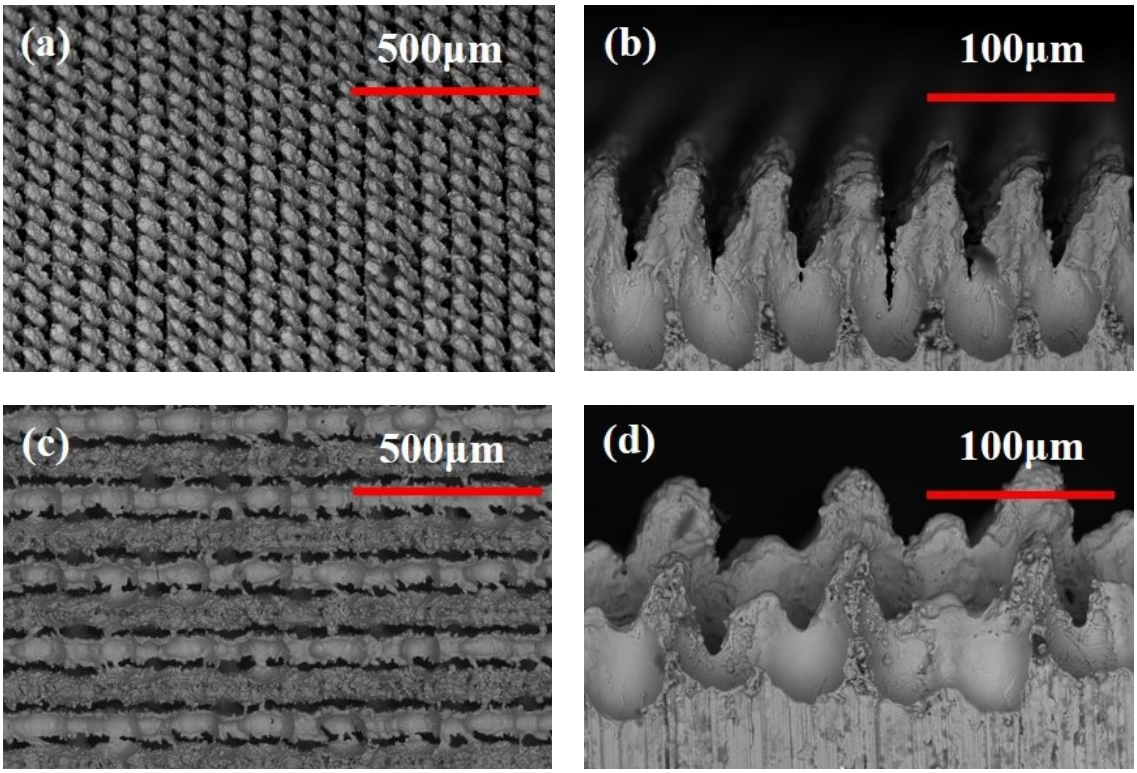

Figure 5.2 Laser Machined Samples: (a) Top View of Pillar Design, (b) Side View of Pillar Design (c) Top View of Varied Pillar Design, (d) Side View of Varied Pillar Design

Smooth

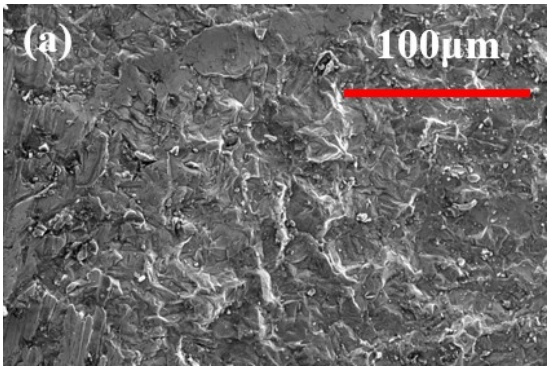

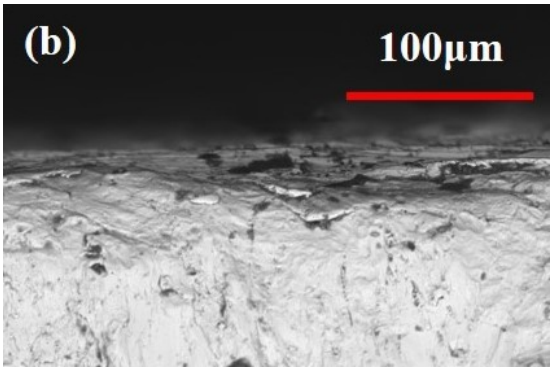

Standoff Distance: 30 mm

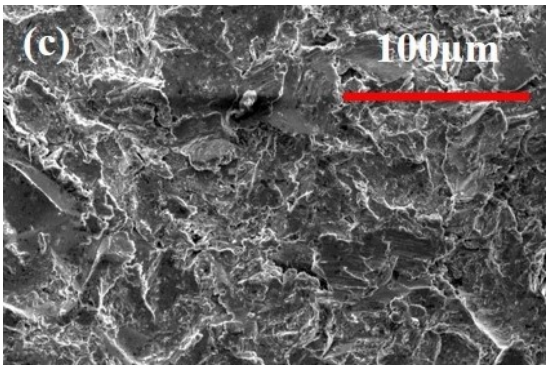

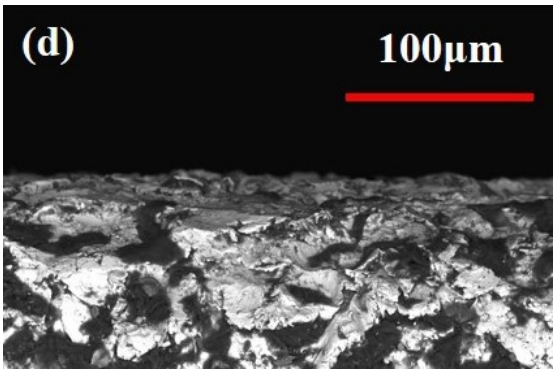

Standoff Distance: 20 mm

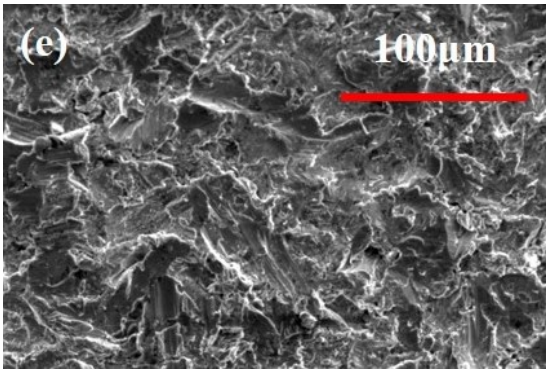

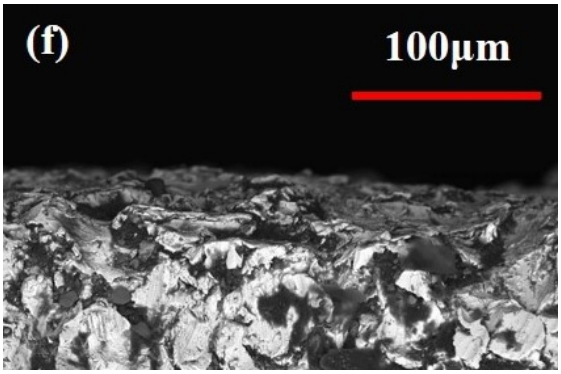

Standoff Distance: 10 mm

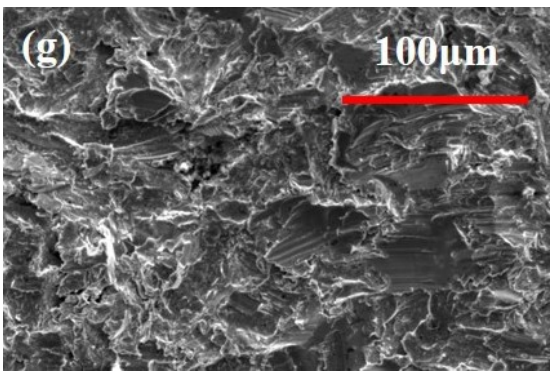

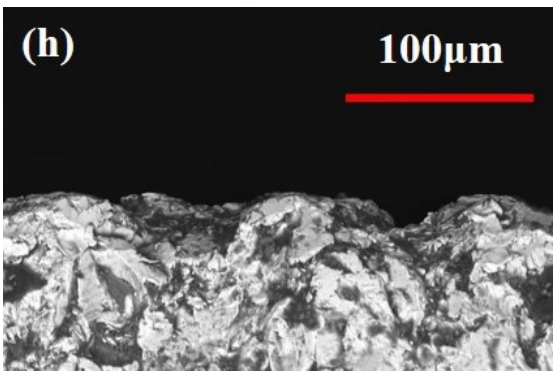

Figure 5.3 Sandblasting Results under Three Different Standoff Distance between Nozzle and Surfaces: 30 mm, 20 mm, 10 mm. The Samples are Made of 17-4 PH Stainless Steel, Pressure 100 psi, Injection Angle 90° (Left Column is Top View, Right Column is Side View)

5.3 Contact Angle and Hysteresis Results Comparison

From Figure 5.4 (a), the coating group is overall higher than uncoated group in contact angle. Before coating, the two laser-treated samples: pillar and varied pillar show better hydrophobicity than the sandblasted samples made under different standoff distances. Within the sandblasted samples, the static contact angle results are very close for the samples made under 10 mm and 20 mm which are better than the samples made under 30 mm. Sandblasted samples made under 10 mm standoff distance can reach 113°±4° without any coating compared with static contact angle 128°±5° from laser-machined sample (pillar). After coating, the contact angle of sandblasted sample is 137°±3° compared with 142°±5° from pillar design. The coating method narrows the differences between them.

(a)

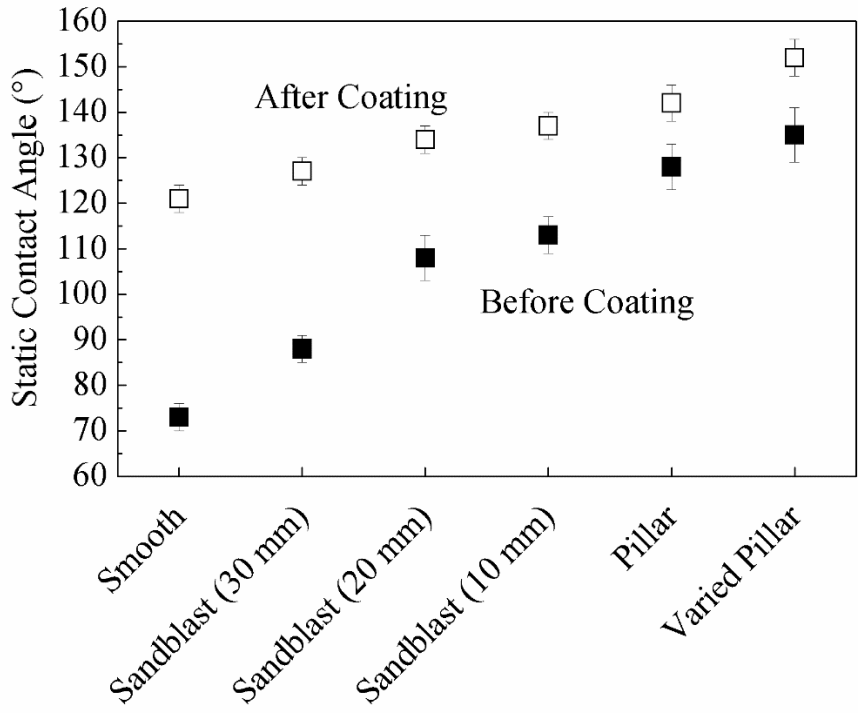

(b)

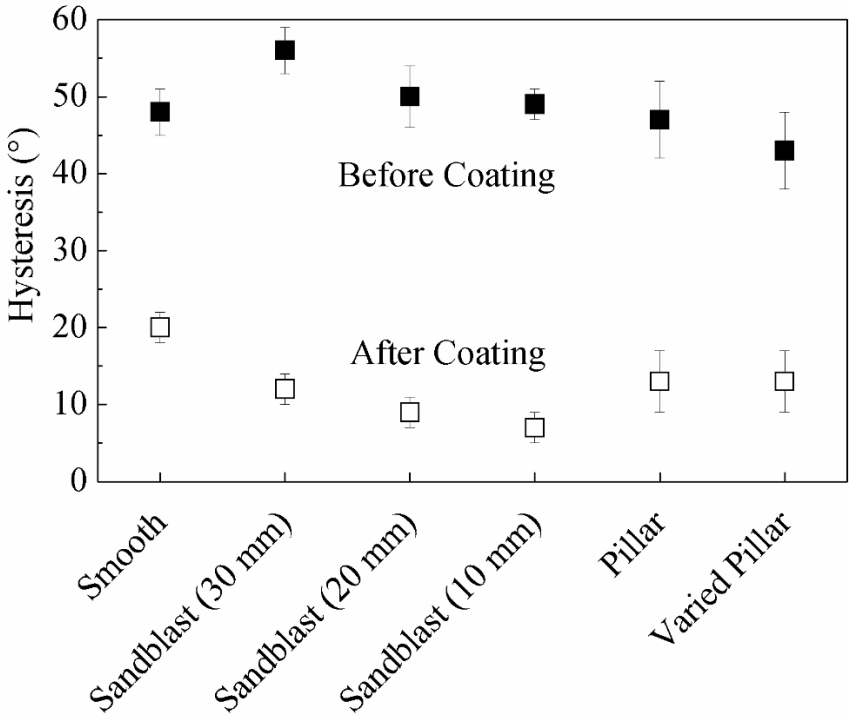

Figure 5.4 Comparison of Laser-machining Samples: Pillar and Varied Pillar and Sandblasting Samples under Three Different Standoff Distance between Nozzle and Surfaces: 30 mm, 20 mm, 10 mm. (a) Contact Angle Results Divided into Coated Group and Uncoated Group, (b) Hysteresis Results Divided into Coated Group and Uncoated Group.

For hysteresis results as shown in Figure 5.4 (b), coating method is still effective and lower the hysteresis in the coating group compared with the uncoated group. But the difference between contact angle results and hysteresis results is that the hysteresis values are much closer than contact angle values. Before coating, the hysteresis results are nearly equal for the two methods. After coating, hysteresis results of sandblasted samples are lower than the results of laser-machined samples. Sandblasted samples made under 10 mm and 20 mm still show more similarity than the samples fabricated under 30 mm. For the laser machined samples after coating, no obvious difference in the hysteresis is found between pillar and varied pillar.

5.4 Discussion

Coating effect

Coating is applied on both laser-treated samples and sandblasted samples. The coating group is overall better than the uncoated group in both static contact angle and hysteresis results.

Structure effect (laser and sandblast)

In Eq. (2.2), r is the roughness ratio which is defined as the ratio of real surface area to projected surface area. In practice, r is a constant that always higher than 1 because real surface area is always larger than projected surface area due to structure existence. According to the Wenzel model, contact angle will be higher with microscale structures on a surface if the original contact angle of a smooth surface is larger than 90°. On the contrary, contact angle will decrease with microscale structures if the original contact angle is smaller than 90°. In other words, surface structure can increase hydrophobicity if the original surface is hydrophobic and increase hydrophilicity if the original surface is hydrophilic.

In this case, the original contact angle (smooth) is 73°±3°. With microscale structures either by laser machining or sandblasting, the contact angles of the samples are higher than 90°, so the Wenzel model is not applicable. In this case, the Cassie model is more suitable as shown in Eq. (2.3). According to the Cassie model, higher contact angle can be only obtained at lower f_1. As $f_1 + f_2 = 1$, f_2 will be larger which means top droplet contacts more air part per unit area after making structures. The air part underneath top liquid is also called air pockets. In the Cassie model, lower f_1 or higher f_2 can help to increase contact angle. In other words, more contact with air or air pockets can help to increase contact angle.

Hysteresis is also based on structures besides surface energy [117]. During adding volume into a droplet, it will pin along its triple phase contact line for a while before its moving [118]. At

the “pin” moment, the free-energy barrier between metastable state and the stable state must be overcome before wetting more surface [119]. For a random structured surface, a triple phase contact line covers both solid part and air part. The hysteresis value is based on the droplet pinning on both solid part and liquid part. The water adhesion on air part are much smaller than that on solid part [120]. As discussed in static contact angle analysis, the higher static contact angle usually caused by larger air part in unit area. For sandblasted samples made under 30 mm, its air part is smaller than the samples made under 10 mm and 20 mm, the result is consistent with the assumption related to air part. For the laser-machined samples, the top parts are heavily deformed to cone shape. The structure defect may result in the high hysteresis.

For the two laser-treated samples: pillar and varied pillar, their contact angles are higher than the sandblasted samples under different standoff distances. From laser samples results, contact angle and hysteresis results measured from perpendicular to grooves and parallel to grooves are very close. So, the droplet deformed by structure can be neglected in this case. Pillar and varied pillar show better contact angle performance than smooth sample perhaps because of micron structure from laser. Liquid may not invade into the gaps among the pillars if partial air is trapped to form “air pockets”. The trapped air phenomenon may happen at both large scale (≈100μm) in laser-machined samples and small scale (≈10μm) in sandblasted samples. Air pockets effect could play an important role in static contact angle. Roughness is one way to explain the difference among different samples but it is not sufficient. Possible reasons may be from sub-micron structure influence from laser and chemical change under high temperature change under laser machining. Not all rough surfaces can lead to repellent property. Many roughened structures can also result in Wenzel state which lower contact angle compare with original surface. Sandblasted surface may contain both Cassie’s state structure and Wenzel’s state structure. Sandblasted samples have random topography compared with laser-machined pseudo-regular microstructure. Sandblasting method showed similar ability to achieve

hydrophobicity compared with laser method. Considering mass production ability of sandblasting method, sandblasting method may be a potential solution to achieve mass production of hydrophobic surface.

From sandblast samples results, topographic features of sandblasted samples contain both cracks and plastic deformation. The static contact angle results of 10 mm and 20 mm samples are very close and better than 30 mm sample. Because lower standoff distance can provide higher impact energy, deeper structure could be made under higher impact energy. Contact angle and hysteresis measured from four directions are very close. The droplet deformed by structure can be neglected in this case. After coating, hysteresis values of sandblasted samples are lower than those laser-machined samples.

5.5 Summary

In this research, sandblasted samples under three different standoff distances (10 mm, 20 mm, 30 mm) were compared with two laser-machined samples with pillar and varied pillar structures. The process of sandblasting and laser machining was compared. The efficiency of sandblasting can be increased by enlarging the nozzle size. It's is easier to achieve mass production in sandblasting with a larger spray range than line-by-line machining with laser. The SEM images show that the edges of samples made under 10 mm and 20 mm standoff distance are more fluctuant than those under 30 mm. According to the static contact angle and hysteresis results, the coating group is better than the uncoated group. Sandblasted samples can reach 113°±4° without any coating compared with static contact angle of 128°±5° from laser-machined sample (pillar). After coating, the contact angle of sandblasted sample is 137°±3° compared with 142°±4° from pillar design. In hysteresis measurement, the results are nearly equal for the two methods before coating. After coating, hysteresis values of sandblasted samples are lower than those from laser-machined samples. The static contact angle and

hysteresis results are likely controlled by surface roughness, and affected by the sub-micron structure.

Chapter 6

Conclusions and Future Work

6.1 Conclusions

Mass production of hydrophobic surface is a great challenge. Laser machining and sandblasting methods to fabricate hydrophobic surface are discussed in this thesis. Wettability study and scanning electron microscope (SEM) research have been done to compare the surfaces from the two fabrication methods. Static contact angle and hysteresis are used to represent their wettability. The impact brought by various microstructures from laser machining work and different standoff distances in sandblasting work are the focuses of this thesis.

The literature review covered different fabrication methods and main applications of hydrophobic surfaces. Also reviewed are influential factors on wettability, three important wetting models, and different contact angle measurement methods.

Main conclusions from this research are summarized as follows:

- In laser machining study, four surfaces with microstructures from laser machining show hydrophobicity without any coating. The values based on mm-sized water droplets of these contact angles, all near 130 °, are consistent with a simple Cassie-Baxter model for wetting that assumes only fractional surface area contact between the droplet and the surface. The original smooth surface is set as control on which water contact angle is 73°±3°. After coating, all laser-machined samples show higher static contact angle and lower hysteresis.
- Sandblasted surfaces with relatively small features (<10 μm) produce hydrophobic

responses for mm-sized water droplets. For stainless steel, lower standoff distance between the nozzle and the surface showed better hydrophobicity. Sandblasting increases wettability of the carbon steel samples, with lower contact angle from lower standoff distance. One possible explanation for this phenomenon is that the concentration of created micro coves or cracks is different for the two materials. After applying Aculon coating, the values of contact angles are all over 120°. The hysteresis for all coated samples are dramatically decreased compared to the ones without coating.

- The comparison between laser machining and sandblasting is conducted on three aspects, i.e., fabrication mechanism, surface structure (SEM images), and wettability. The efficiency of sandblasting can be increased by adjusting the nozzle size. With a larger spray range, mass production of hydrophobic surface is more possible than line-by-line laser machining. From SEM images, the edge of samples made with 10 mm and 20 mm distances are more fluctuant than the samples made under the standoff distance of 30 mm. According to static contact angle and hysteresis results, samples in the coating group are better than those in the uncoated group. Sandblasted samples can reach 113°±4° without any coating, compared with static contact angle 128°±5° from laser-machined samples (pillar design). After coating, the contact angle of sandblasted samples is 137°±3° compared with 142°±5° from laser machined samples with pillar. In hysteresis measurement, the results are nearly equal for the two methods before coating. After coating, hysteresis values of sandblasted samples are lower than laser-machined samples.

6.2 Future Work

Several suggestions related to this thesis work are shown below for further investigation:

- Besides microstructures in large scale (≈100 μm) from laser machining, small scales (<10 μm) can be fabricated via chemical deposition or micro-EDM to investigate the scale impacts on wettability and compare the wettability performances with microstructure in large scales.
- For sandblasting research, the blast media is Aluminum Oxide in 45-140 Mesh Size. Abrasive particles types, particle size and injection angle are some factors that can be tested in the future.
- For wettability study, as shown in 2.4, there are other methods to measure dynamic contact angles, i.e., the Wilhelmy method and captive bubble method. These methods can be used and the contact angle measurement results can be compared with the results from the sessile drop method used in this research.
- In this thesis, submicron structures were found in laser machining work. Nano coves can also affect static contact angle and hysteresis. This can be further studied by Atomic Force Microscope.

References

[1] Peng, K., & Xinxin, W. (2011). Super-cooled Large Droplets consideration in the droplet impingement simulation for aircraft icing. Procedia Engineering, 17, 151-159.

[2] Karmouch, R., Coudé, S., Abel, G., & Ross, G. G. (2009, October). Icephobic PTFE coatings for wind turbines operating in cold climate conditions. In Electrical Power & Energy Conference (EPEC), 2009 IEEE (pp. 1-6). IEEE.

[3] Cao, L., Jones, A. K., Sikka, V. K., Wu, J., & Gao, D. (2009). Anti-icing superhydrophobic coatings. Langmuir, 25(21), 12444-12448.

[4] Nishimoto, S., & Bhushan, B. (2013). Bioinspired self-cleaning surfaces with superhydrophobicity, superoleophobicity, and superhydrophilicity. Rsc Advances, 3(3), 671-690.

[5] Lu, Y., Sathasivam, S., Song, J., Crick, C. R., Carmalt, C. J., & Parkin, I. P. (2015). Robust self-cleaning surfaces that function when exposed to either air or oil. Science, 347(6226), 1132-1135.

[6] Tian, H., Zhang, J., Wang, E., Yao, Z., & Jiang, N. (2015). Experimental investigation on drag reduction in turbulent boundary layer over superhydrophobic surface by TRPIV. Theoretical and Applied Mechanics Letters, 5(1), 45-49.

[7] Truesdell, R., Mammoli, A., Vorobieff, P., van Swol, F., & Brinker, C. J. (2006). Drag reduction on a patterned superhydrophobic surface. Physical review letters, 97(4), 044504.

[8] Chen, F., Zhang, D., Yang, Q., Yong, J., Du, G., Si, J., ... & Hou, X. (2013). Bioinspired wetting surface via laser microfabrication. ACS applied materials & interfaces, 5(15), 6777-6792.

[9] Yilbas, B. S., Malik, J., & Patel, F. (2014). Laser gas assisted treatment of AISI H12 tool steel and corrosion properties. Optics and Lasers in Engineering, 54, 8-13.

[10] Prashanth, K. G., Debalina, B., Wang, Z., Gostin, P. F., Gebert, A., Calin, M., ... & Eckert, J. (2014). Tribological and corrosion properties of Al–12Si produced by selective laser melting. Journal of Materials Research, 29(17), 2044-2054.

[11] Tang, M. K., Huang, X. J., Guo, Z., Yu, J. G., Li, X. W., & Zhang, Q. X. (2015). Fabrication of robust and stable superhydrophobic surface by a convenient, low-cost and efficient laser marking approach. Colloids and Surfaces A: Physicochemical and Engineering Aspects, 484, 449-456.

[12] Martínez-Calderon, M., Rodríguez, A., Dias-Ponte, A., Morant-Minana, M. C., Gómez-Aranzadi, M., & Olaizola, S. M. (2016). Femtosecond laser fabrication of highly hydrophobic stainless steel surface with hierarchical structures fabricated by combining ordered microstructures and LIPSS. Applied Surface Science, 374, 81-89.

[13] Liang, C., Li, B., Wang, H., Li, B., Yang, J., Zhou, L., ... & Li, C. (2014). Preparation of hydrophobic and oleophilic surface of 316 L stainless steel by femtosecond laser irradiation in water. Journal of Dispersion Science and Technology, 35(9), 1345-1350.

[14] SLĂTINEANU, L., POTÂRNICHE, Ş., COTEAŢĂ, M., GRIGORAŞ, I., GHERMAN, L., & NEGOESCU, F. (2011). Surface roughness at aluminium parts sand blasting. Proceedings in Manufacturing Systems, 6(2).

[15] Paredes, R. S. C., Amico, S. C., & d'Oliveira, A. S. C. M. (2006). The effect of roughness and pre-heating of the substrate on the morphology of aluminium coatings deposited by thermal spraying. Surface and Coatings Technology, 200(9), 3049-3055.

[16] Beckford, S., & Zou, M. (2011). Micro/nano engineering steel substrates to produce superhydrophobic surfaces. Thin Solid Films, 520(5), 1520-1524.

[17] Ruiz-Cabello, F. J. M., Amirfazli, A., Cabrerizo-Vílchez, M., & Rodríguez-Valverde, M. A. (2016). Fabrication of water-repellent surfaces on galvanized steel. RSC Advances, 6(76), 71970-71976.

[18] Wong, Y. S., Rahman, M., Lim, H. S., Han, H., & Ravi, N. (2003). Investigation of micro-EDM material removal characteristics using single RC-pulse discharges. Journal of Materials Processing Technology, 140(1), 303-307.

[19] Bae, W. G., Song, K. Y., Rahmawan, Y., Chu, C. N., Kim, D., Chung, D. K., & Suh, K. Y. (2012). One-step process for superhydrophobic metallic surfaces by wire electrical discharge machining. ACS applied materials & interfaces, 4(7), 3685-3691.

[20] Weisensee, P. B., Torrealba, E. J., Raleigh, M., Jacobi, A. M., & King, W. P. (2014). Hydrophobic and oleophobic re-entrant steel microstructures fabricated using micro electrical discharge machining. Journal of Micromechanics and Microengineering, 24(9), 095020.

[21] Sun, S. X., Xie, R., Wang, X. X., Wen, G. Q., Liu, Z., Wang, W., ... & Chu, L. Y. (2015). Fabrication of nanofibers with phase-change core and hydrophobic shell, via coaxial electrospinning using nontoxic solvent. Journal of materials science, 50(17), 5729-5738.

[22] Miyauchi, Y., Ding, B., & Shiratori, S. (2006). Fabrication of a silver-ragwort-leaf-like super-hydrophobic micro/nanoporous fibrous mat surface by electrospinning. Nanotechnology, 17(20), 5151.

[23] Han, J. T., Zheng, Y., Cho, J. H., Xu, X., & Cho, K. (2005). Stable superhydrophobic organic− inorganic hybrid films by electrostatic self-assembly. The Journal of Physical Chemistry B, 109(44), 20773-20778.

[24] Zhao, Y., Tang, Y., Wang, X., & Lin, T. (2010). Superhydrophobic cotton fabric fabricated by electrostatic assembly of silica nanoparticles and its remarkable buoyancy. Applied Surface Science, 256(22), 6736-6742.

[25] Li, X., Du, X., & He, J. (2010). Self-cleaning antireflective coatings assembled from peculiar mesoporous silica nanoparticles. Langmuir, 26(16), 13528-13534.

[26] Qu, B., Wang, J., Pan, L., Pan, C., Zhou, X., & Gu, Z. (2011). Bionic duplication of fresh navodon septentrionalis fish surface structures. Journal of Nanomaterials, 2011.

[27] Karaman, M., Çabuk, N., Özyurt, D., & Köysüren, Ö. (2012). Self-supporting superhydrophobic thin polymer sheets that mimic the nature's petal effect. Applied Surface Science, 259, 542-546.

[28] Sun, G., Fang, Y., Zhi, H., & Li, Z. (2015). Biomimetic fabrication of polymer film with high adhesive superhydrophobicity by duplicating locust wing surface. Chemical Research in Chinese Universities, 31(5), 895-898.

[29] Yu, Q., Zeng, Z., Zhao, W., Li, H., Wu, X., & Xue, Q. (2013). Patterned tailored hydrophobic films designed by synergy effect of electrochemical deposition and chemical deposition. Chemical Communications, 49(24), 2424-2426.

[30] Hang, T., Hu, A., Ling, H., Li, M., & Mao, D. (2010). Super-hydrophobic nickel films with micro-nano hierarchical structure prepared by electrodeposition. Applied Surface Science, 256(8), 2400-2404.

[31] He, G., & Wang, K. (2011). The super hydrophobicity of ZnO nanorods fabricated by electrochemical deposition method. Applied Surface Science, 257(15), 6590-6594.

[32] Ishizaki, T., Hieda, J., Saito, N., Saito, N., & Takai, O. (2010). Corrosion resistance and chemical stability of super-hydrophobic film deposited on magnesium alloy AZ31 by

microwave plasma-enhanced chemical vapor deposition. Electrochimica Acta, 55(23), 7094-7101.

[33] Gurav, A. B., Latthe, S. S., Kappenstein, C., Mukherjee, S. K., Rao, A. V., & Vhatkar, R. S. (2011). Porous water repellent silica coatings on glass by sol–gel method. Journal of Porous Materials, 18(3), 361-367.

[34] Nadargi, D. Y., Gurav, J. L., El Hawi, N., Rao, A. V., & Koebel, M. (2010). Synthesis and characterization of transparent hydrophobic silica thin films by single step sol–gel process and dip coating. Journal of Alloys and Compounds, 496(1), 436-441.

[35] Mahadik, S. A., Mahadik, D. B., Kavale, M. S., Parale, V. G., Wagh, P. B., Barshilia, H. C., ... & Rao, A. V. (2012). Thermally stable and transparent superhydrophobic sol–gel coatings by spray method. Journal of sol-gel science and technology, 63(3), 580-586.

[36] Minami, T., Mayama, H., Nakamura, S., Yokojima, S., Shen, J. W., & Tsujii, K. (2008). Formation mechanism of fractal structures on wax surfaces with reference to their super water-repellency. Soft Matter, 4(1), 140-144.

[37] Wang, J., Monton, M. R. N., Zhang, X., Filipe, C. D., Pelton, R., & Brennan, J. D. (2014). Hydrophobic sol–gel channel patterning strategies for paper-based microfluidics. Lab on a Chip, 14(4), 691-695.

[38] Drelich, J., & Chibowski, E. (2010). Superhydrophilic and superwetting surfaces: definition and mechanisms of control. Langmuir, 26(24), 18621-18623.

[39] Pawar, S. S., & Sunnapwar, V. K. (2013). Experimental studies on heat transfer to Newtonian and non-Newtonian fluids in helical coils with laminar and turbulent flow. Experimental Thermal and Fluid Science, 44, 792-804.

[40] Bierwagen, G. P., He, L., Li, J., Ellingson, L., & Tallman, D. E. (2000). Studies of a new accelerated evaluation method for coating corrosion resistance—thermal cycling testing. Progress in Organic Coatings, 39(1), 67-78.

[41] Gavili, A., Zabihi, F., Isfahani, T. D., & Sabbaghzadeh, J. (2012). The thermal conductivity of water base ferrofluids under magnetic field. Experimental Thermal and Fluid Science, 41, 94-98.

[42] Zhang, X., Tian, J., Wang, L., & Zhou, Z. (2002). Wettability effect of coatings on drag reduction and paraffin deposition prevention in oil. Journal of Petroleum Science and Engineering, 36(1), 87-95.

[43] Samimi, A., & Zarinabadi, S. (2011). An Analysis of Polyethylene Coating Corrosion in Oil and Gas Pipelines. Journal of American science, USA.

[44] Tiratsoo, J. N. H. (1992). Pipeline pigging technology. Gulf Professional Publishing.

[45] Guo, B., Song, S., Ghalambor, A., & Chacko, J. (2005). Offshore Pipelines. Elsevier.

[46] Gogte, S., Vorobieff, P., Truesdell, R., Mammoli, A., van Swol, F., Shah, P., & Brinker, C. J. (2005). Effective slip on textured superhydrophobic surfaces. Physics of fluids, 17(5), 51701-51701.

[47] Choi, C. H., & Kim, C. J. (2006). Large slip of aqueous liquid flow over a nanoengineered superhydrophobic surface. Physical review letters, 96(6), 066001.

[48] Dai, Q., Huang, W., & Wang, X. (2014). Surface roughness and orientation effects on the thermo-capillary migration of a droplet of paraffin oil. Experimental Thermal and Fluid Science, 57, 200-206.

[49] Huang, K., Wan, J. W., Chen, C. X., Li, Y. Q., Mao, D. F., & Zhang, M. Y. (2013). Experimental investigation on friction factor in pipes with large roughness. Experimental Thermal and Fluid Science, 50, 147-153.

[50] Doidjo, M. T., Belec, L., Aragon, E., Joliff, Y., Lanarde, L., Meyer, M., ... & Perrin, F. X. (2013). Influence of silane-based treatment on adherence and wet durability of fusion bonded epoxy/steel joints. Progress in Organic Coatings, 76(12), 1765-1772.

[51] Ou, J., Perot, B., & Rothstein, J. P. (2004). Laminar drag reduction in microchannels using ultrahydrophobic surfaces. Physics of Fluids (1994-present), 16(12), 4635-4643.

[52] Daniello, R. J., Waterhouse, N. E., & Rothstein, J. P. (2009). Drag reduction in turbulent flows over superhydrophobic surfaces. Physics of Fluids (1994-present), 21(8), 085103.

[53] Liu, W., Sun, D., Li, C., Liu, Q., & Xu, J. (2006). Formation and stability of paraffin oil-in-water nano-emulsions prepared by the emulsion inversion point method. Journal of Colloid and Interface Science, 303(2), 557-563.

[54] Bannwart, A. C., Rodriguez, O. M., de Carvalho, C. H., Wang, I. S., & Vara, R. M. (2004). Flow patterns in heavy crude oil-water flow. Journal of energy resources technology, 126(3), 184-189.

[55] Miwa, M., Nakajima, A., Fujishima, A., Hashimoto, K., & Watanabe, T. (2000). Effects of the surface roughness on sliding angles of water droplets on superhydrophobic surfaces. Langmuir, 16(13), 5754-5760.

[56] Petrie, H. L., Deutsch, S., Brungart, T. A., & Fontaine, A. A. (2003). Polymer drag reduction with surface roughness in flat-plate turbulent boundary layer flow. Experiments in Fluids, 35(1), 8-23.

[57] Angeli, P., & Hewitt, G. F. (1999). Pressure gradient in horizontal liquid–liquid flows. International Journal of Multiphase Flow, 24(7), 1183-1203.

[58] Teisala, H., Tuominen, M., & Kuusipalo, J. (2011). Adhesion mechanism of water droplets on hierarchically rough superhydrophobic rose petal surface. Journal of Nanomaterials, 2011, 33.

[59] Yuan, Z., Chen, H., & Zhang, J. (2008). Facile method to prepare lotus-leaf-like super-hydrophobic poly (vinyl chloride) film. Applied Surface Science, 254(6), 1593-1598.

[60] Butt, H. J., Graf, K., & Kappl, M. (2006). Physics and chemistry of interfaces. John Wiley & Sons.

[61] Románszki, L., Mohos, M., Telegdi, J., Keresztes, Z., & Nyikos, L. (2014). A comparison of contact angle measurement results obtained on bare, treated, and coated alloy samples by both dynamic sessile drop and Wilhelmy method. Periodica Polytechnica. Chemical Engineering, 58(Supplement), 53.

[62] Hong, S. J., Chang, F. M., Chou, T. H., Chan, S. H., Sheng, Y. J., & Tsao, H. K. (2011). Anomalous contact angle hysteresis of a captive bubble: advancing contact line pinning. Langmuir, 27(11), 6890-6896.

[63] Szyszka, D. (2014). Measurement of contact angle of copper-bearing shales using the captive bubble method. Mining Science, 21.

[64] Jung, J. W. and Wan, J. 2012. Supercritical CO_2 and ionic strength effects on wettability of silica surfaces: Equilibrium contact angle measurements. *Energy & Fuels*, 26(9), 6053-6059.

[65] Sghaier, N., Prat, M., and Nasrallah, S. B. 2006. On the influence of sodium chloride concentration on equilibrium contact angle. *Chemical Engineering Journal*, 122(1), 47-53.

[66] Saraji, S., Piri, M., and Goual, L. 2014. The effects of SO_2 contamination, brine salinity, pressure, and temperature on dynamic contact angles and interfacial tension of supercritical CO 2/brine/quartz systems. *International Journal of Greenhouse Gas Control*, 28, 147-155.

[67] Extrand, C. W., & Moon, S. I. 2010. When sessile drops are no longer small: Transitions from spherical to fully flattened. *Langmuir*, 26(14), 11815-11822.

[68] Artus, G. R., Jung, S., Zimmermann, J., Gautschi, H. P., Marquardt, K., and Seeger, S. 2006. Silicone nanofilaments and their application as superhydrophobic coatings. *Advanced Materials*, 18(20), 2758-2762.

[69] Groenendijk, M. 2008. Fabrication of super hydrophobic surfaces by fs laser pulses. *Laser Technik Journal*, 5(3), 44-47.

[70] Bhushan, B., and Jung, Y. C. 2006. Micro-and nanoscale characterization of hydrophobic and hydrophilic leaf surfaces. *Nanotechnology*, 17(11), 2758.

[71] Sarmadivaleh, M., Al-Yaseri, A. Z., & Iglauer, S. (2015). Influence of temperature and pressure on quartz–water–CO 2 contact angle and CO 2–water interfacial tension. Journal of colloid and interface science, 441, 59-64.

[72] Young, T. (1805). An essay on the cohesion of fluids. Philosophical Transactions of the Royal Society of London, 95, 65-87.

[73] Wenzel, R. N. (1949). Surface roughness and contact angle. The Journal of Physical Chemistry, 53(9), 1466-1467.

[74] Cassie, A. B. D., & Baxter, S. (1944). Wettability of porous surfaces. Transactions of the Faraday society, 40, 546-551.

[75] Gao, L., & McCarthy, T. J. (2006). Contact angle hysteresis explained. Langmuir, 22(14), 6234-6237.

[76] Kusumaatmaja, H., & Yeomans, J. M. (2007). Modeling contact angle hysteresis on chemically patterned and superhydrophobic surfaces. Langmuir, 23(11), 6019-6032.

[77] Marmur, A. (1998). Contact-angle hysteresis on heterogeneous smooth surfaces: theoretical comparison of the captive bubble and drop methods. Colloids and Surfaces A: Physicochemical and Engineering Aspects, 136(1-2), 209-215.

[78] Öpik, U. (2000). Contact-angle hysteresis caused by a random distribution of weak heterogeneities on a solid surface. Journal of colloid and interface science, 223(2), 143-166.

[79] Xiu, Y., Zhu, L., Hess, D. W., & Wong, C. P. (2008). Relationship between work of adhesion and contact angle hysteresis on superhydrophobic surfaces. The Journal of Physical Chemistry C, 112(30), 11403-11407.

[80] Eral, H. B., & Oh, J. M. (2013). Contact angle hysteresis: a review of fundamentals and applications. Colloid and polymer science, 291(2), 247-260.

[81] Vedantam, S., & Panchagnula, M. V. (2008). Constitutive modeling of contact angle hysteresis. Journal of colloid and interface science, 321(2), 393-400.

[82] Kulinich, S. A., & Farzaneh, M. (2009). Effect of contact angle hysteresis on water droplet evaporation from super-hydrophobic surfaces. Applied Surface Science, 255(7), 4056-4060.

[83] Yeh, K. Y., Chen, L. J., & Chang, J. Y. (2008). Contact angle hysteresis on regular pillar-like hydrophobic surfaces. Langmuir, 24(1), 245-251.

[84] Zhao, H., Park, K. C., & Law, K. Y. (2012). Effect of surface texturing on superoleophobicity, contact angle hysteresis, and “robustness”. Langmuir, 28(42), 14925-14934.

[85] Jeong, H. E., Kwak, M. K., Park, C. I., & Suh, K. Y. (2009). Wettability of nanoengineered dual-roughness surfaces fabricated by UV-assisted capillary force lithography. Journal of

colloid and interface science, 339(1), 202-207.

[86] Gad-el-Hak, M., "Compliant coatings for drag reduction," *Progress in Aerospace Sciences*, 38(1), 77-99, (2002).

[87] Zhang, S., Ouyang, X., Li, J., Gao, S., Han, S., Liu, L., & Wei, H., "Underwater Drag Reducing Effect of Superhydrophobic Submarine Model," Langmuir, 31(1), 587-593, (2014).

[88] Mohd, M. H., & Paik, J. K., "Investigation of the corrosion progress characteristics of offshore subsea oil well tubes," Corrosion Science, 67, 130-141, (2013).

[89] Wang, Shutao, et al. "Bioinspired surfaces with superwettability: new insight on theory, design, and applications." Chemical Reviews 115.16 (2015): 8230-8293.

[90] Wenzel, R. N., "Resistance of solid surfaces to wetting by water," *Industrial & Engineering Chemistry*, 28(8), 988-994, (1936).

[91] Cassie, A. B. D. and Baxter, S., "Wettability of porous surfaces," *Transactions of the Faraday Society*, 40, 546-551, (1944).

[92] Crawford, R. J., & Ivanova, E. P, *Superhydrophobic Surfaces*, Elsevier, pp. 141–157, (2015).

[93] Chen, F., Zhang, D., Yang, Q., Yong, J., Du, G., Si, J., & Hou, X., "Bioinspired wetting surface via laser microfabrication," ACS applied materials & interfaces, 5(15), 6777-6792, (2013).

[94] Vorobyev, A. Y., and Chunlei Guo. "Multifunctional surfaces produced by femtosecond laser pulses." Journal of Applied Physics 117.3 (2015): 033103.

[95] Wang, X. C., Wu, L. Y., Shao, Q., and Zheng, H. Y., "Laser micro structuring on a Si substrate for improving surface hydrophobicity," Journal of Micromechanics and

Microengineering, 19(8), 085025, (2009).

[96] Bizi-Bandoki, P., Benayoun, S., Valette, S., Beaugiraud, B., and Audouard, E., "Modifications of roughness and wettability properties of metals induced by femtosecond laser treatment," Applied Surface Science, 257(12), 5213-5218, (2011).

[97] Dahotre, N. B., Paital, S. R., Samant, A. N., and Daniel, C., "Wetting behaviour of laser synthetic surface microtextures on Ti–6Al–4V for bioapplication. Philosophical Transactions of the Royal Society of London A: Mathematical," Physical and Engineering Sciences, 368(1917), 1863-1889, (2010).

[98] Chen, F., Zhang, D., Yang, Q., Wang, X., Dai, B., Li, X., & Hou, X., "Anisotropic wetting on microstrips surface fabricated by femtosecond laser," Langmuir, 27(1), 359-365, (2010).

[99] Groenendijk, M., "Fabrication of super hydrophobic surfaces by fs laser pulses," Laser Technik Journal, 5(3), 44-47, (2008).

[100] Bhushan, B. and Jung, Y. C., "Micro-and nanoscale characterization of hydrophobic and hydrophilic leaf surfaces," Nanotechnology, 17(11), 2758, (2006).

[101] Canay, Ş., Kocadereli, I., & Akça, E. (2000). The effect of enamel air abrasion on the retention of bonded metallic orthodontic brackets. American Journal of Orthodontics and Dentofacial Orthopedics, 117(1), 15-19.

[102] Shkodkin, A., Kashirin, A., Klyuev, O., & Buzdygar, T. (2006). Metal particle deposition stimulation by surface abrasive treatment in gas dynamic spraying. Journal of Thermal Spray Technology, 15(3), 382-386.

[103] Marmur, A. (2008). From hygrophilic to superhygrophobic: theoretical conditions for making high-contact-angle surfaces from low-contact-angle materials. Langmuir, 24(14), 7573-7579.

[104] Liu, K., Yao, X., & Jiang, L. (2010). Recent developments in bio-inspired special wettability. Chemical Society Reviews, 39(8), 3240-3255.

[105] Xiu, Y., Zhu, L., Hess, D. W., & Wong, C. P. (2007). Hierarchical silicon etched structures for controlled hydrophobicity/superhydrophobicity. Nano letters, 7(11), 3388-3393.

[106] Lampin, M., Warocquier-Clérout, R., Legris, C., Degrange, M. F. (1997). Correlation between substratum roughness and wettability, cell adhesion. Journal of biomedical materials research, 36(1), 99-108.

[107] Ourahmoune, R., Salvia, M., Mathia, T. G., & Mesrati, N. (2014). Surface morphology and wettability of sandblasted PEEK. Scanning, 36(1), 64-75.

[108] Varacalle, D. J., Guillen, D. P., Deason, D. M., Rhodaberger, W., & Sampson, E. (2006). Effect of grit-blasting on substrate roughness and coating adhesion. Journal of Thermal Spray Technology, 15(3), 348-355.

[109] Kim, D., Kim, J., Park, H. C., Lee, K. H., & Hwang, W. (2007). A superhydrophobic dual-scale engineered lotus leaf. Journal of Micromechanics and Microengineering, 18(1), 015019.

[110] Barranco, V., Onofre, E., Escudero, M. L., & Garcia-Alonso, M. (2010). Characterization of roughness and pitting corrosion of surfaces modified by blasting and thermal oxidation. Surface and Coatings Technology, 204(23), 3783-3793.

[111] Che-Shun, W. A. N. G., Ker-Kong, C. H. E. N., Tajima, K., Nagamatsu, Y., Kakigawa, H., & Kozono, Y. (2010). Effects of sandblasting media and steam cleaning on bond strength of titanium-porcelain. Dental materials journal, 29(4), 381-391.

[112] Albakry, M., Guazzato, M., & Swain, M. V. (2004). Effect of sandblasting, grinding, polishing and glazing on the flexural strength of two pressable all-ceramic dental materials. Journal of dentistry, 32(2), 91-99.

[113] Aktas, G., Sahin, E., Vallittu, P., Özcan, M., & Lassila, L. (2013). Effect of colouring

green stage zirconia on the adhesion of veneering ceramics with different thermal expansion coefficients. International journal of oral science, 5(4), 236-241.

[114] Cuypers, P. A., Hermens, W. T., & Hemker, H. C. (1977). Ellipsometric study of protein film on chromium. Annals of the New York Academy of Sciences, 283(1), 77-85.

[115] McCafferty, E., & Wightman, J. P. (1997). Determination of the surface isoelectric point of oxide films on metals by contact angle titration. Journal of colloid and interface science, 194(2), 344-355.

[116] Kim, H. S., Kang, W. S., & Hong, S. H. (2010). Metal surface treatment for enhancement of hydrophilic property using atmospheric-pressure dielectric barrier discharge. IEEE Transl. Plasma Sci, 38, 1982.

[117] Ebert, D., & Bhushan, B. (2012). Durable Lotus-effect surfaces with hierarchical structure using micro-and nanosized hydrophobic silica particles. Journal of colloid and interface science, 368(1), 584-591.

[118] Dorrer, C., & Rühe, J. (2006). Advancing and receding motion of droplets on ultrahydrophobic post surfaces. Langmuir, 22(18), 7652-7657.

[119] Giacomello, A., Schimmele, L., & Dietrich, S. (2016). Wetting hysteresis induced by nanodefects. Proceedings of the National Academy of Sciences, 113(3), E262-E271.

[120] Liu, M., Wang, S., Wei, Z., Song, Y., & Jiang, L. (2009). Bioinspired design of a superoleophobic and low adhesive water/solid interface. Advanced Materials, 21(6), 665-669.